Critical state line of copper tailings under different loading types: mineralogy effect

RODRIGO ZORZAL VELTEN*, MATHEW RICHARD COOP†, MAIKI MAFESSOLI‡, JOÃO PAULO RODRIGUES DA COSTA§, CARLOS ALEX ALVES LIMA‖, JOÃO VÍTOR DE AZAMBUJA CARVALHO# and NILO CESAR CONSOLI**

Mining tailings can have mineralogy distinct from natural soils due to their anthropogenic nature. However, the effects of mineralogy on the critical state response of tailings have not yet been studied without the influence of grading. The reasons for differences in the critical state line (CSL) shape and position of geomaterials remain unclear, since the effects of gradation, mineralogy, loading type, particle size, shape and fabric are not well understood. Accordingly, this paper focuses on the effect of mineralogy on the CSL of copper tailings by evaluating two silty-sand tailings. Although these geomaterials exhibit similar gradations, they differ substantially in mineralogy. Triaxial compression tests under three degrees of compaction and four effective confining pressure values (ranging from 50 to 400 kPa) were performed and compared to published results under simple shear conditions. One copper tailings presented non-unique CSLs depending on the initial fabric and loading path, while the other exhibited unique CSLs regardless of the initial density or loading condition. The results also revealed the influence of mineralogy on the critical state parameter M, with the micaceous tailings presenting a lower critical state friction angle than the tectosilicate-rich one.

KEYWORDS: fabric/structure of soils; geotechnical engineering; mineralogy; simple shear; tailings; tailings storage facilities; triaxial tests

INTRODUCTION

The growing global demand for minerals and metals across all sectors of the economy and industry has been responsible for the increase in annual ore production. However, most mines currently explored worldwide are low-grade ore deposits, particularly those for extraction of base metals, such as gold, silver, copper and nickel, among others. Consequently, the main challenge faced by the mining industry is the management of tailings, by-products from the beneficiation activities. In the coming years, a massive volume of tailings will have to be stored and managed by mining companies (Bowker & Chambers, 2017; Islam & Murakami, 2021).

In this context, tailings dams have been the preferred method for storing tailings for operational and economic reasons. Although tailings dams have been built to ensure that tailings are safely stored, protecting the natural environment from degradation, when they fail, the resulting effects greatly and negatively impact the planet, the economy and people, known as the triple bottom line (Byrne *et al.*, 2018; Islam & Murakami, 2021). Since the frequency of failure of tailings storage facilities (TSFs) has been higher than that of other infrastructure, the research interest in tailings has substantially grown, with the aim of enhancing current knowledge on tailings behaviour and proposing alternatives to the disposal of tailings in conventional dams.

The characteristics of tailings, such as their composition, particle morphology and grading, depend on the characteristics of the parent ore and can be highly variable. Specifically, the mineralogy of the particles can greatly influence the geomaterial's expected behaviour (Nakata *et al.*, 2001; Nocilla *et al.*, 2019; Zhang *et al.*, 2020; Consoli *et al.*, 2024). For instance, Bolton (1986) demonstrated that the critical state friction angle of quartzitic sands is slightly lower than that of feldspathic sands. In contrast, quartz- and feldspar-originated sand presents higher shear strength than micaceous sands.

Mineralogy also exerts influence on the shape of the critical state line (CSL) in the compression plane (v–log p'). Although the shape and position of the CSL of tailings have usually been related to their grading (e.g. Li & Coop, 2019; Secco *et al.*, 2026), Velten *et al.* (2025) found that two copper tailings with similar gradings presented curved or linear CSLs related to their composition. In addition, uncommon mineralogy has been associated with the occurrence of 'transitional' behaviour (Nocilla *et al.*, 2006, 2019; Coop, 2015). Transitional soils present strong forms of fabric that persist after large strains, ultimately leading to a group of semi-parallel CSLs depending on the initial fabric.

Investigation of the transitional response and the influence of mineralogy on geomaterials' behaviour has primarily been conducted for triaxial compression conditions. However, the conditions imposed in these geotechnical

Manuscript received 21 December 2025; revised manuscript accepted 30 June 2026.

Discussion on this paper closes six months after article publication; for further details see p. ii.
* Universidade Federal do Rio Grande do Sul, Porto Alegre, Brazil (Orcid:0000-0002-3179-3416).
† Department of Civil, Environmental & Geomatic Engineering, University College London, London, UK (Orcid:0000-0002-3301-552X).
‡ Graduate Programme in Civil Engineering, Universidade Federal do Rio Grande do Sul, Porto Alegre, Brazil (Orcid:0009-0004-8295-3741).
§ RTFE Base Metals South Atlantic, VALE, Parauapebas, Brazil.
‖ Salobo Mine, VALE, Parauapebas, Brazil.
Graduate Programme in Civil Engineering, Universidade Federal do Rio Grande do Sul, Porto Alegre, Brazil (Orcid:0000-0002-7555-5022).
** Graduate Programme in Civil Engineering, Universidade Federal do Rio Grande do Sul, Porto Alegre, Brazil (Orcid:0000-0002-6408-451X) (corresponding author: ncconsoli@gmail.com).

tests are different from those often found in the field (Wagner *et al*., 2023). Consequently, there is a lack of data on the geomechanical response of tailings under different types of loading, with a few exceptions of studies using the hollow cylinder (e.g. Sadrekarimi, 2016; Fanni *et al*., 2024) and the direct simple shear (DSS) (e.g. Riveros & Sadrekarimi, 2021; Karim *et al*., 2023) apparatuses. It is also important to mention the research conducted by Riemer & Seed (1997), which evaluated the effect of the level of consolidation stress, the drainage conditions and the effective stress path on the apparent position of the steady-state line of loose, saturated sands under triaxial compression and simple shear loadings.

Therefore, this paper addresses the influence of mineralogy and stress path on the shape, position and uniqueness of the CSL of two silty-sand copper tailings by comparing triaxial compression results with the simple shear data of Velten *et al*. (2025). The tailings share a similar particle size distribution while each retains distinct mineralogy. Triaxial tests of copper tailings compacted at different initial void ratios were conducted under confining pressures ranging from 50 to 400 kPa to evaluate possible 'transitional' response, which can cause severe problems to the stability of TSFs if not properly identified.

EXPERIMENTAL PROGRAMME

The copper tailings used in this study are the same as those used by Velten *et al*. (2025), who conducted undrained simple shear tests. Here, complementary mineralogical and morphological tests were conducted since the focus of the work is the influence of microscale characteristics on the macro scale response. Eighteen monotonic drained compression triaxial tests and 17 monotonic undrained compression triaxial tests were conducted.

Materials

Since this study focuses on evaluating the effect of mineralogy, the tailings are identified as CoT (copper tailings rich in tectosilicates) and CoP (copper tailings rich in phyllosilicates), referring to the different minerals they present. Fig. 1 shows the grain size distribution of both tailings and pictures of samples for the simple shear and triaxial tests of both geomaterials. Table 1 summarises the main physical characteristics of each material.

Table 1. Physical properties of copper tailings

Parameters	CoT	CoP
	Total tailings	Total tailings
Specific gravity, G_s	2·814	3·149
Gravel: %	0·00	0·00
Coarse sand: %	0·00	0·00
Medium sand: %	1·55	0·00
Fine sand: %	50·98	57·70
Total sand: %	52·53	57·70
Silt: %	37·44	33·70
Clay: %	10·03	8·60
Mean particle size, D_{50}: mm	0·082	0·082
Uniformity coefficient, C_u	26·7	15·9
Coefficient of curvature, C_{cr}	1·7	5·1
LL: %	—	—
IP: %	Non-plastic	Non-plastic
ASTM – USCS classification	SM	SM
Standard Proctor optimum moisture content, w_{opt}: %	12·76	14·43
Standard Proctor maximum dry density, $\gamma_{d\max}$: kN/m^3	18·49	19·02
Modified Proctor optimum moisture content, w_{opt}: %	10·40	10·25
Modified Proctor maximum dry density, $\gamma_{d\max}$: kN/m^3	19·44	21·13
Maximum void ratio: e_{max}	1·479	2·044
Minimum void ratio: e_{min}	0·420	0·462

The particle size distribution was obtained by way of sieve and sedimentation analysis according to ASTM D6913 (ASTM, 2017a) and ASTM D7928 (ASTM, 2021a), respectively. The specific gravity was assessed following the ASTM D854 (ASTM, 2014) procedures, and the Atterberg limits were evaluated according to ASTM D4318 (ASTM, 2017b). Both tailings are silty sands (SM), according to the Unified Soil Classification System (ASTM, 2017c). Also, they are classified as well-graded materials (C_u > 5) and present similar gradings with an identical D_{50}.

Figure 2 displays the compaction curves at standard (ASTM, 2021b) and modified (ASTM, 2021c) efforts, in terms of the void ratios of both tailings, which clearly offer some insight into the arrangements and fabric produced when compacting different materials (Wagner *et al*., 2025). From Fig. 2, the difference between the modified and the normal minimum void ratio obtained for each optimum water content is close to 0·16 for CoP and 0·07 for CoT.

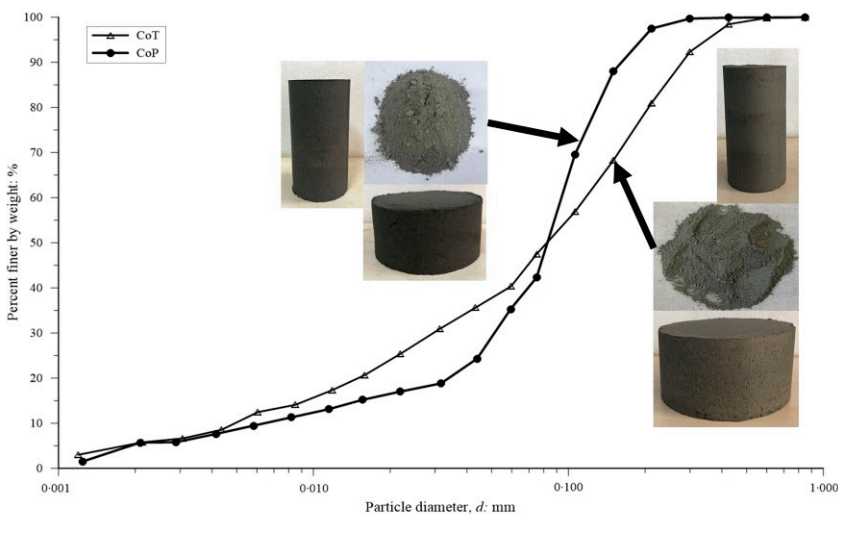

Fig. 1. Particle size distribution of the total copper tailings samples

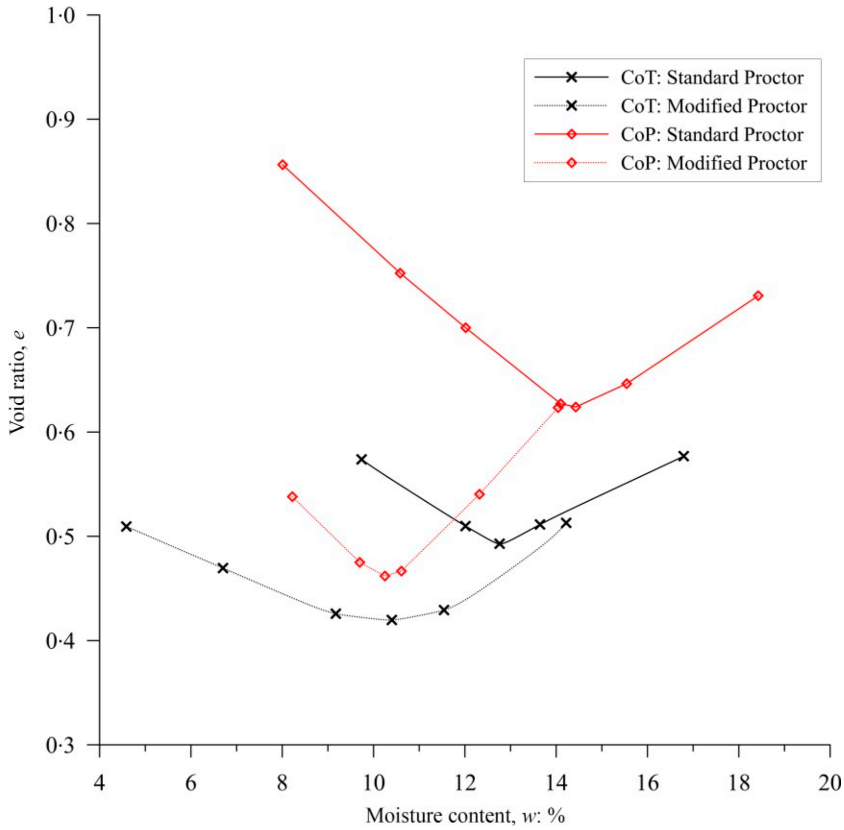

Fig. 2. Compaction characteristics of copper tailings samples. Compaction curves in terms of void ratio

This result can be attributed to differences in the packing of grains, since CoT exhibits bulky particles and CoP flat ones, as will be discussed below. The lower void ratio of CoT does not represent a denser state, however, which can be further confirmed by the similar relative density values (93% for CoT at the optimum compaction point for standard energy and 90% for CoP under the same conditions).

Mineralogical and morphological aspects. Figure 3 presents the quantitative determination of minerals in both copper tailings studied and their scanning electron microscopy (SEM) analysis. The qualitative evaluation of minerals by scanning electron microscopy (QEMSCAN) method was adopted for this purpose, which is based on SEM analysis and a mineral database. This analysis verified that CoT is constituted mainly by tectosilicates (17·9% quartz and 36·7% albite/feldspar, totalling 54·6%). In turn, CoP is composed of tectosilicates (16·4% quartz and 8·3% albite/feldspar, totalling 24·7%) and phyllosilicates (24·3% biotite – mica group – and 15·8% chlorite – chlorite group, totalling 40·1%).

Geologically, the two tailings differ due to the formation processes of their parent rocks. On the one hand, CoT derives from the beneficiation of copper ore bodies encountered in a shear zone established in the contact between metavolcanic sedimentary units and trondhjemitic and tonalitic gneisses. On the other hand, CoP is the by-product of the processing of ore bodies that derive from foliated (or shale aspects) rocks (Teixeira & Lindenmayer, 2012).

As can be seen in Fig. 3, CoT mainly consists of bulky particles with some flocs around, typical of tectosilicates, while CoP presents flocculent (foliated) particles, typical of phyllosilicates, with some flocs bridging bulky particles (Chang *et al.*, 2011). Also, CoP presents biotite particles forming, ordering, bridging and pore-filling microstructures, in agreement with the schematic representations of the microstructure of mica mixed with classical and residual soils proposed by Zhang *et al.* (2024).

Methods

Moulding of specimens. The testing specimens were moulded considering three different degrees of compaction (i.e. 86, 91 and 95%) established based on the compaction characteristics (Fig. 2) of standard Proctor effort, which is the most common compaction energy adopted in earthworks, especially for mining geotechnical structures. The standard optimum moisture content was used for both tailings regardless of degree of compaction ($w_{op} = 12·76\%$ for CoT and $w_{op} = 14·43\%$ for CoP). For CoT tailings, the moulding void ratio values were 0·736 (86S), 0·641 (91S) and 0·572 (95S); for CoP tailings, 0·889 (86S), 0·785 (91S) and 0·710 (95S), in which 86, 91 and 95 represent the three different degrees of compaction adopted and 'S' means standard, referring to standard Proctor compaction effort. The moist tamping technique (e.g. Frost & Park, 2003; Corrêa & Oliveira Filho, 2019) was used to prepare the specimens for all tests.

For simple shear tests, the specimens' dimensions, moulding procedures and test specifications are presented in Velten *et al.* (2025) and are omitted here for the sake of brevity. For triaxial compression tests, moist tailings layers were deposited inside a split mould and manually tamped to the assigned specific volume following the undercompaction method (Ladd, 1978). Three layers were used in this process, with the tops of the first and second layers scarified to guarantee better adherence to the subsequent layer. Figs 4(a) and 4(b) present photographs of dense specimens of CoT (presenting strain localisation) and CoP, respectively, at the end of drained triaxial compression tests under an effective confining pressure of 50 kPa. From those

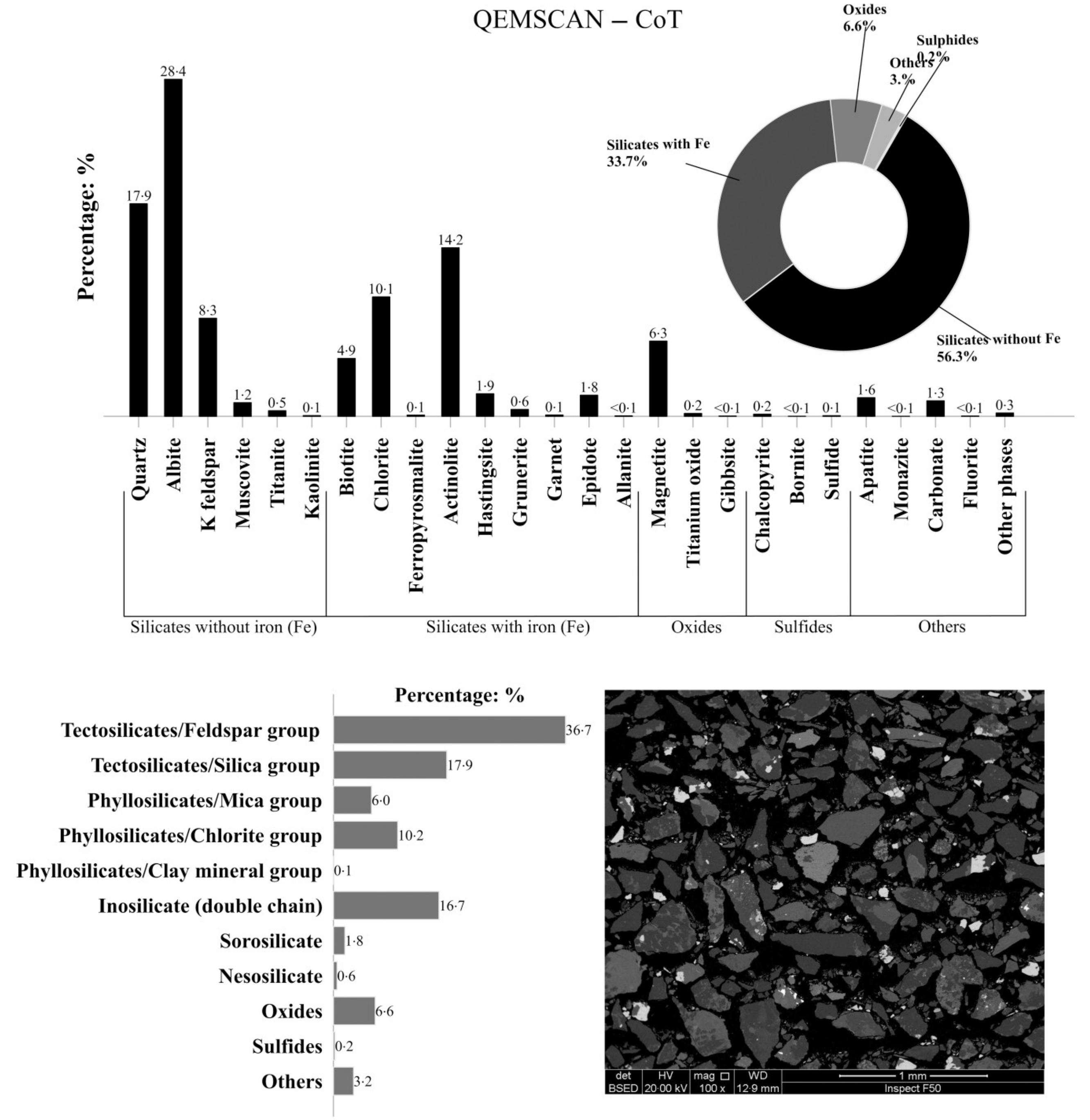

(a)

Fig. 3. Qualitative and quantitative mineralogical analysis using QEMSCAN technique, with grains morphology from SEM analysis: (a) CoT – minerals detected from darkest to lightest grey tone: quartz, albite, K feldspar, scapolite, actinolite, biotite, hastingsite, magnetite and chalcopyrite; and (b) CoP – minerals detected from darkest to lightest grey tone: quartz, biotite, garnet, magnetite and sulfides

pictures, the uniformity of specimens moulded for the test can be verified. The continuous line represents the location of the base and top of the specimen, and the dashed line represents the location of Hall effect sensors glued over the rubber membrane surface.

It is important to highlight that significant particle breakage is not expected to occur during the moulding process. Velten *et al*. (2025) have shown that the same tailings used here presented minimal particle breakage during oedometric compression up to stresses much higher than those promoted in the moulding procedure. As discussed by Wagner *et al*. (2024), particle breakage has been more directly associated with the stress state experienced by the sample than the load frequency, requiring much higher stress to observe a significant change in grading.

Triaxial testing programme. Isotropically consolidated drained (CID) and undrained (CIU) triaxial compression tests were undertaken to assess the geomechanical response of the two compacted copper tailings under confining pressures spanning from 50 to 400 kPa. In total, 35 triaxial compression tests were conducted, considering both materials, and these are summarised in Table 2 (CoT) and Table 3 (CoP). The nomenclature of the tests was given by

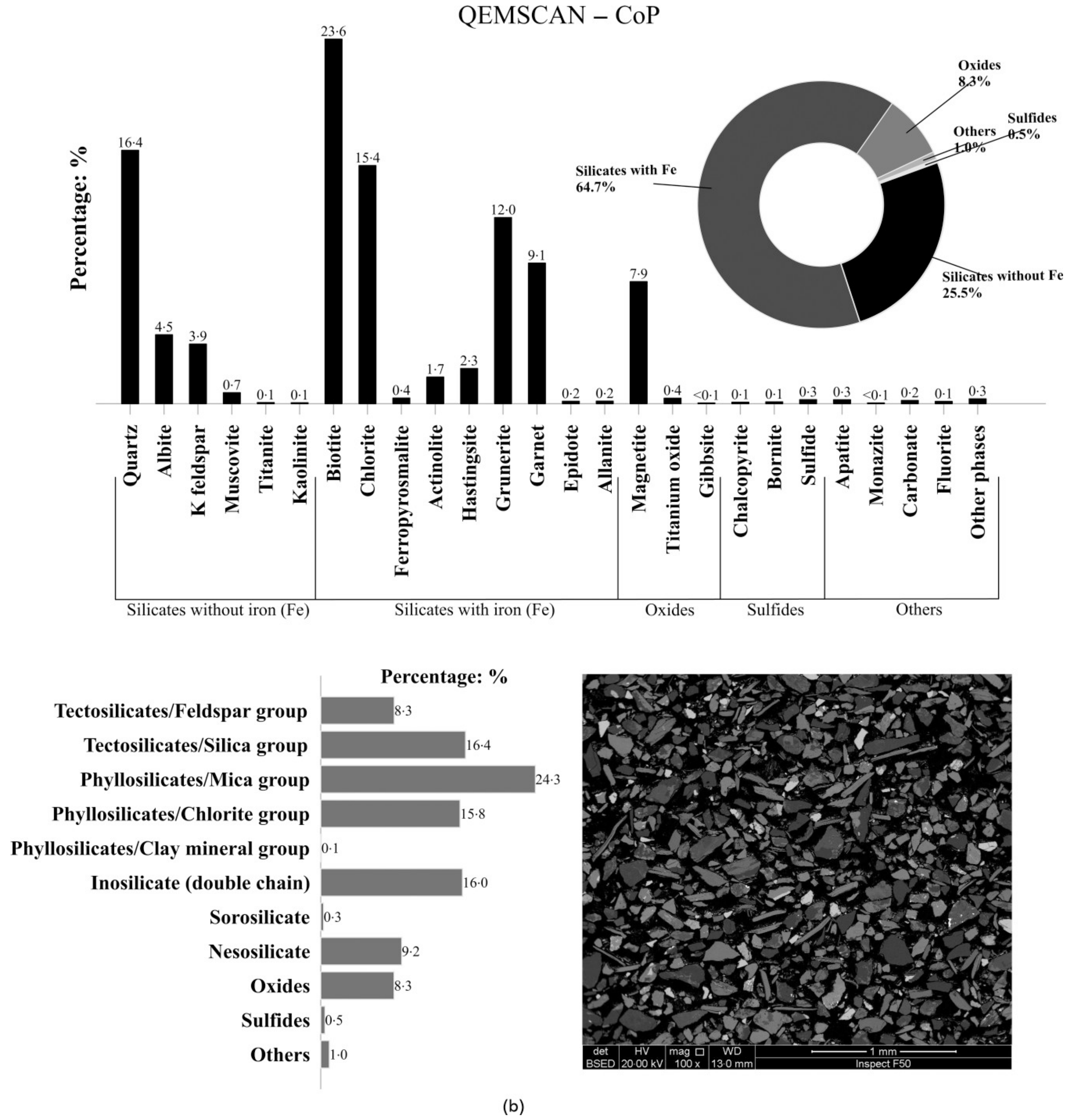

Fig. 3. continued

A_BC_D kPa, in which 'A' is the material studied (e.g. CoT or CoP), 'B' refers to the type of triaxial compression test (e.g. D for drained test and U for undrained), 'C' refers to degree of compaction of the specimen (e.g. 95S) and 'D' is the initial effective confining pressure of the test (e.g. 100 kPa).

The tests followed the recommendations of ASTM D7181 (ASTM, 2020a) and ASTM D4767 (ASTM, 2020b) standards. First, the specimens were submitted to a saturation process composed of carbon dioxide percolation, water percolation and incrementally increasing backpressure to achieve 400 kPa (keeping the mean effective stress equal to 20 kPa). Skempton *B* values were measured after saturation and were all greater than 0·98. Then, the consolidation phase was conducted by incrementing the chamber pressure up to the desired p'_0 value.

Finally, the shearing phase was carried out using a strain-controlled method with a rate of 4·32 mm/h for both tests (e.g. CID and CIU) to guarantee a better stress distribution inside the specimen. Also, two Hall effect sensors were used to evaluate the axial displacements, and one was employed to measure the radial displacements (Clayton & Khatrush, 1986). These sensors were fundamental to calculating axial and radial displacements in all stages of the test. The specimen's dimensions and moisture content at the end of the test were measured, aiming to obtain the void ratio through the most independent forms as possible (Shipton & Coop, 2015). Although end-of-test soil freezing (Reid *et al*., 2021; Sladen & Handford, 1987) was not used, the measurement of the final moisture content of saturated samples has demonstrated good agreement and sufficient accuracy (Murthy *et al*., 2007; Shipton & Coop, 2015),

(a) (b)

Fig. 4. Photographs of dense specimens at the end of the drained triaxial compression test at an effective confining pressure of 50 kPa (continuous line indicates the base and top positions of the specimen; dashed line indicates the positions of Hall effect sensors): (a) CoT_D95S_50 kPa and (b) CoP_D95S_50 kPa. Photographs were taken with membrane to preserve water content determination at the end of the test

particularly when used in conjunction with internal measurements.

RESULTS AND DISCUSSION

Influence of mineralogy on the triaxial compression response of copper tailings

Tables 2 and 3 summarise the main characteristics of undrained and drained triaxial compression tests on CoT and CoP tailings, respectively. Fig. 5(a) (drained monotonic triaxial compression tests) and Fig. 5(b) (undrained monotonic triaxial compression tests) present the results on CoT and CoP tailings.

Under drained conditions (Fig. 5(a)), both copper tailings presented a strain-hardening response to the end of the test, except for the densest CoT specimen under the lowest confining stress (CoT_D95S_50 kPa), which exhibited the formation of a shear band (see Fig. 4(a)). However, CoT exhibited a stiffer response than CoP. Except for the densest specimen of CoT tailings under the lowest confining stress (CoT_D95S_50 kPa), all tests presented contractive volumetric strains despite their compaction degree. In addition, differences were verified for the M values obtained for CoT ($M = 1{\cdot}46$) and for CoP ($M = 1{\cdot}40$). Considering that they present similar gradation, the differences observed in M might be associated with their considerable mineralogical differences.

On the undrained geomechanical response (Fig. 5(b)), CoT tailings specimens exhibited a well-defined peak strength followed by a strain-softening response in the deviatoric stress–axial strain diagram. Considerable loss of strength was verified for loose (86S) and medium (91S) states at an effective confining pressure of 100 kPa, indicating the occurrence of static liquefaction. These results are confirmed in the excess pore pressure response for CoT copper tailings (also shown in Fig. 5(b)) – that is, considerable positive excess pore pressure was generated during undrained tests at degrees of compaction of 86% (86S) and 91% (91S). However, negative excess pore pressure values were generated for the densest specimen under 100 kPa (low) confining stress (CoT_U95S_100 kPa). In contrast, CoP tailings specimens presented a ductile response (increasing axial strain, deviatoric stress increased – or kept about constant) with positive pore pressure generation (as also presented in Fig. 5(b)), and undrained instability was not observed. These undrained responses also agree with the monotonic geomechanical response data that Seethalakshmi & Sachan (2020) reported for pure and micaceous sands of Sabarmati soil. In addition, Fig. 5(c) portrays the $q/(Mp')$–dilatancy (D) of both tailings, in which M is M_{CoT} (for CoT tailings) or M_{CoP} (for CoP tailings).

Figure 6 compares the response of CoT and CoP tailings presenting similar void ratios initially and prior to shear and under the same confining pressure. Under drained loading conditions, small differences were obtained in the deviatoric stress–axial strain response (Fig. 6(a)), but the CoT specimen presented larger volumetric strains than the CoP specimen. Under undrained loading conditions (Fig. 6(b)), the CoP specimen presented a ductile response, while the CoT specimen liquefied (Fig. 6(b)).

Influence of loading direction on the response of copper tailings

Figures 7 and 8 display the stress paths for CoT and CoP tailings, respectively. The end-of-test points are highlighted for each material and for each type of loading studied, and

Table 2. Summary of triaxial compression test data, CoT

Test	p'_0: kPa	p'_{peak}: kPa	q_{peak}: kPa	p'_{cs}: kPa	q_{cs}: kPa	ψ_{c}	v_0	v_{c}	v_{sh}
CoT_U86S_100 kPa	100	106.	110·5	3·4	4·4	0·06	1·72	1·72	1·72
CoT_U86S_200 kPa	200	150·7	133·3	6·8	4·4	0·07	1·72	1·71	1·71
CoT_U91S_100 kPa	100	102·8	116·8	6·5	1·9	0·03	1·65	1·64	1·64
CoT_U91S_200 kPa	200	199·9	221·6	35·9	39·1	0·03	1·64	1·63	1·63
CoT_U91S_400 kPa	400	267·7	267·3	76·1	94·0	0·04	1·69	1·62	1·62
CoT_U95S_50 kPa	50	183·6	269·3	156·3	227·5	−0·01	1·58	1·58	1·58
CoT_U95S_100 kPa	100	317·3	457·9	240·6	352·3	−0·01	1·58	1·58	1·58
CoT_U95S_200 kPa	200	346·0	495·2	216·3	314·3	0·00	1·58	1·58	1·58
CoT_D86S_50 kPa	50	95·6	136·8	95·0	135·6	0·05	1·72	1·72	1·66
CoT_D86S_100 kPa	100	188·6	264·3	187·0	259·8	0·06	1·72	1·71	1·64
CoT_D86S_400 kPa	400	791·9	1169·4	786·3	1157·4	0·08	1·71	1·70	1·59
CoT_D91S_50 kPa	50	99·6	149·5	98·3	144·7	0·03	1·65	1·65	1·61
CoT_D91S_100 kPa	100	204·4	307·3	200·4	297·4	0·02	1·65	1·64	1·60
CoT_D91S_400 kPa	400	786·6	1159·2	771·1	1110·5	0·04	1·65	1·63	1·57
CoT_D95S_50 kPa	50	99·8	150·8	93·5	132·1	−0·01	1·58	1·58	1·59
CoT_D95S_100 kPa	100	192·3	274·9	190·2	266·9	−0·01	1·58	1·58	1·58
CoT_D95S_400 kPa	400	781·2	1143·2	767·9	1103·9	0·00	1·58	1·57	1·55

Table 3. Summary of triaxial compression test data, CoP

Test	p'_0: kPa	p'_{peak}: kPa	q_{peak}: kPa	p'_{cs}: kPa	q_{cs}: kPa	ψ_c	υ_0	υ_c	υ_{sh}
CoP_U86S_50 kPa	50	39·1	41·5	13·7	26·4	0·09	1·87	1·85	1·85
CoP_U86S_100 kPa	100	71·6	89·5	36·1	68·4	0·08	1·84	1·80	1·80
CoP_U86S_200 kPa	200	115·3	129·8	63·4	100·0	0·09	1·88	1·75	1·75
CoP_U91S_100 kPa	100	69·3	84·4	44·0	67·7	0·04	1·78	1·75	1·75
CoP_U91S_200 kPa	200	124·3	164·4	90·4	136·9	0·05	1·76	1·71	1·71
CoP_U91S_400 kPa	400	222·0	280·0	168·2	238·3	0·06	1·76	1·68	1·68
CoP_U95S_50 kPa	50	104·5	154·7	104·2	154·5	−0·05	1·71	1·71	1·71
CoP_U95S_100 kPa	100	134·7	195·4	127·9	183·0	−0·02	1·70	1·69	1·69
CoP_U95S_200 kPa	200	172·2	241·6	172·2	241·6	0·01	1·69	1·67	1·67
CoP_D86S_50 kPa	50	91·6	125·7	90·9	123·0	0·09	1·87	1·85	1·74
CoP_D86S_100 kPa	100	196·2	290·5	196·4	290·2	0·09	1·85	1·80	1·70
CoP_D86S_400 kPa	400	735·1	1002·8	732·1	995·7	0·09	1·87	1·71	1·59
CoP_D91S_50 kPa	50	89·4	118·1	89·4	118·1	0·01	1·77	1·77	1·72
CoP_D91S_100 kPa	100	191·0	272·6	190·7	272·2	0·04	1·82	1·75	1·65
CoP_D91S_400 kPa	400	767·5	1100·3	766·7	1096·2	0·06	1·83	1·67	1·55
CoP_D95S_50 kPa	50	94·3	130·3	92·4	125·5	−0·05	1·71	1·71	1·70
CoP_D95S_100 kPa	100	191·9	274·5	187·3	261·5	−0·02	1·70	1·70	1·68
CoP_D95S_400 kPa	400	748·5	1038·7	741·0	1021·7	0·02	1·69	1·63	1·56

the respective CSLs are also drawn, with the proper inclination: for simple shear loading, $M = 1{\cdot}02$ for CoT tailings (Fig. 7(a)) and $M = 0{\cdot}99$ for CoP tailings (Fig. 8(a)), while for triaxial compression loading, $M = 1{\cdot}46$ for CoT tailings (Fig. 7(b)) and $M = 1{\cdot}40$ for CoP (Fig. 8(b)).

Notice that the simple shear tests were conducted under full saturation (Skempton's B value higher than 0·95) and with complete knowledge of the specimen's stress state. This was possible due to the use of a non-reinforced latex membrane and the control of confining pressure and back-pressure throughout the test. Further details on the simple shear equipment used and procedures followed can be found in Velten *et al.* (2025).

Equation (1) expresses the relationship between the slope of the CSL in the stress plane, M, and the critical state friction angle, ϕ', for triaxial compression conditions

$$M(\theta = 30^\circ) = M_{tc} = \frac{6 \times \sin(\phi'_{tc})}{3 - \sin(\phi'_{tc})} \quad (1)$$

Velten *et al.* (2025) reported a critical state friction angle under simple shear conditions ($\theta = 0^\circ$), ϕ'_{ss}, for CoT tailings equal to 36·1°; while from equation (1), this geomaterial presents a triaxial compression critical state friction angle, ϕ'_{tc}, equal to 36·0°. In contrast, CoP tailings present ϕ'_{ss} equal to 34·8° (Velten *et al.*, 2025) and ϕ'_{tc} equal to 34·6°.

Regardless of the loading direction, the differences in the critical state friction angle of copper tailings studied herein are mainly related to the mineralogical composition, once they present similar particle size and shape distribution. Bolton (1986) reported that sands containing higher quantities of phyllosilicates from the mica group present lower hardness and, thus, lower critical state friction angle values than quartz–feldspar sands. Nevertheless, the small differences in ϕ'_{tc} and ϕ'_{ss} for both tailings are uncommon. Researchers have systematically reported diverging values for simple shear loading and triaxial compression of sands (e.g. Wroth, 1984; Doherty & Fahey, 2011), with ϕ'_{ss} values being higher.

Moreover, the ratio between M for simple shear (M_{ss}) and triaxial compression (M_{tc}) is approximately 0·7 for both tailings, suggesting a consistent dependence of the critical state strength on the Lode's angle. Although the two tailings exhibit slightly different values of M_{tc}, the similar ratios indicate that mineralogical differences mainly affect the overall strength level rather than the shape of the critical state surface in the deviatoric plane.

Table 4 presents the critical state stress ratio M obtained for each geomaterial and type of loading, and consequently the interpolation function for M in relation to the Lode's angle, $M(\theta)$ – $g(\theta)$ method, proposed by Sheng *et al.* (2000) and Gajo & Muir Wood (1999). This function is expressed in equation (2), in which M_{tc} is the critical stress ratio for triaxial compression, θ is the Lode angle and α is a shape parameter:

$$M(\theta) = M_{tc} \times \left[\frac{2\alpha^4}{(1+\alpha^4) - (1-\alpha^4) \times \sin 3\theta}\right]^{1/4} \quad (2)$$

The $M(\theta)$ curves obtained for both copper tailings (CoT and CoP) are illustrated in Fig. 9, as well as the M values obtained for triaxial compression tests ($\theta = -30^\circ$) and for simple shear tests ($\theta = 0^\circ$). Using this method, it was verified that for both geomaterials the curves presented a smooth transition between different stress paths while maintaining the convexity of the yield surface, as discussed by Matsuoka & Nakai (1974).

Figure 10(a) presents the CSL of CoT tailings under simple shear (Velten *et al.*, 2025) and triaxial compression conditions in the υ–ln p' plane. For CoT tailings, a power-law (curved) relationship (equation (3)) fitted the end-of-tests points, regardless of the loading mode (i.e. simple shear or triaxial compression). However, a single CSL could not fit the data. For triaxial compression, a transitional response was obtained. Thus, the CSL was dependent on the specimen's initial density (Table 5): $a = 1{\cdot}725$ (86S)/1·655 (91S)/1·618 (95S), $b = 0{\cdot}060$ (86S)/0·040 (91S)/0·030 (95S), and $c = 0{\cdot}40$. Conversely, for simple shear loading, a power-law (curved) CSL could fit all end-of-test data, regardless of the specimen's initial density (in the υ–ln p' plane) (Table 5): $a = 1{\cdot}720$, $b = 0{\cdot}121$ and $c = 0{\cdot}55$.

$$\upsilon = \mathrm{a} - b \times \left(\frac{p'}{p'_{ref}}\right)^c$$

In the case of CoP tailings, Fig. 11(a) presents a unique log-linear CSL (equation (4)) that could fit the end-of-test points of all initial states and loading modes. These results are also summarised in Table 5, while Table 6 presents the regression analysis results for all (CoT and CoP) the CSLs calculated. These data have shown that the values for the

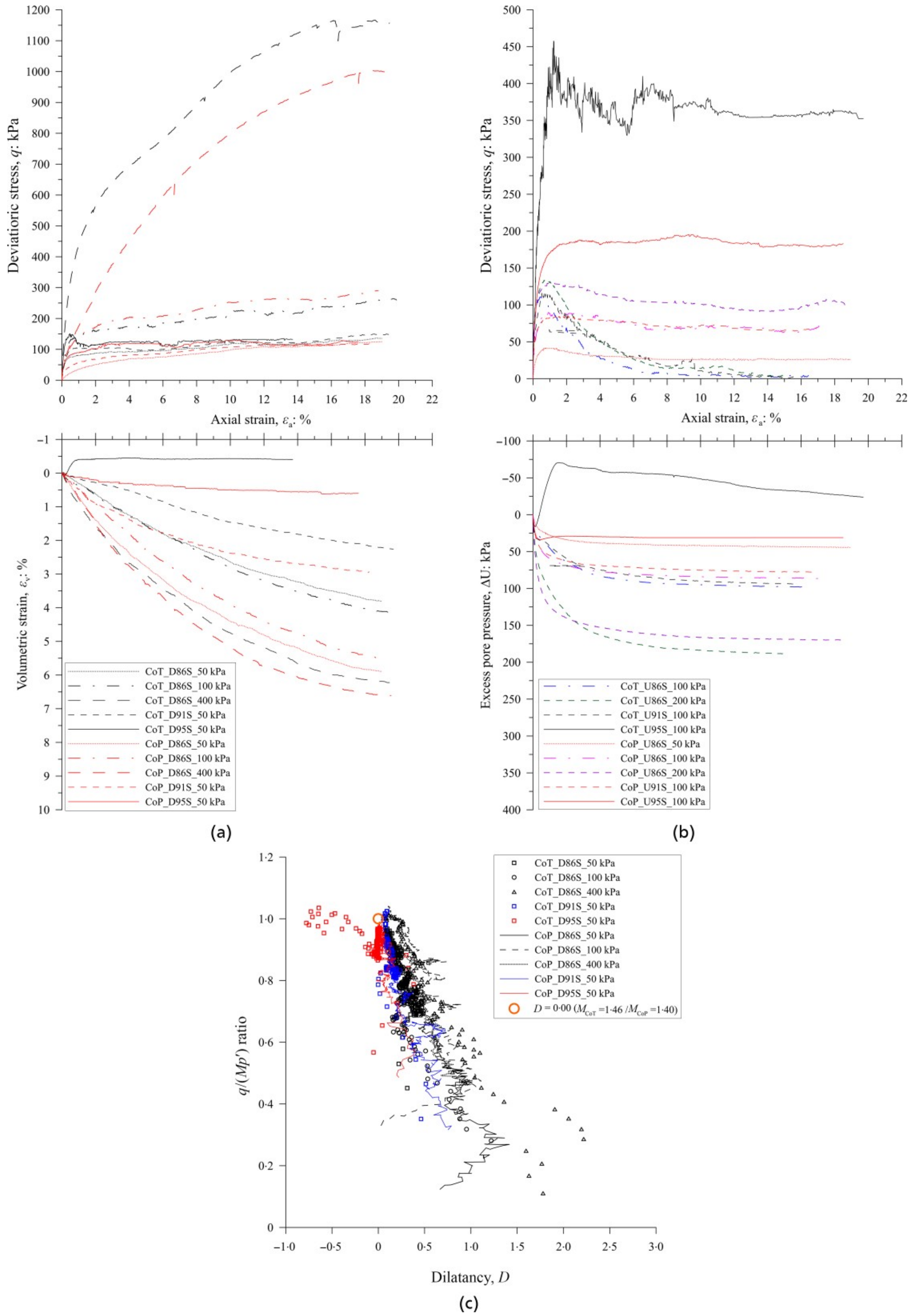

Fig. 5. CoT and CoP triaxial compression tests: (a) drained tests – D: deviatoric stress–axial strain–volumetric strain; (b) undrained tests – U: deviatoric stress–axial strain–excess pore pressure; and (c) dilatancy, D–(η/M_{CoT} and η/M_{CoP})

coefficient of determination R^2 obtained were acceptable (i.e. equal to or higher than 0·95) and the p-values calculated were lower than 0·001.

$$\upsilon = \Gamma + \lambda \ln p' \quad (4)$$

From Fig. 10(a), CoT presents ‘transitional’ behaviour under triaxial compression loading conditions, but not for simple shear conditions. It means that, in this case, transitionality depends on the loading mode. On the other side, CoP (Fig. 11(a)) presents a unique CSL independently of the specimen’s initial density (i.e. fabric) and type of loading. Consequently, these differences can probably be related to mineralogical aspects and fabric instead of the type of loading, since CoP presents higher quantities of minerals with foliated/sheet format, for example micas, while CoT presents higher quantities of minerals with massive rotund particles, for example quartz and feldspars.

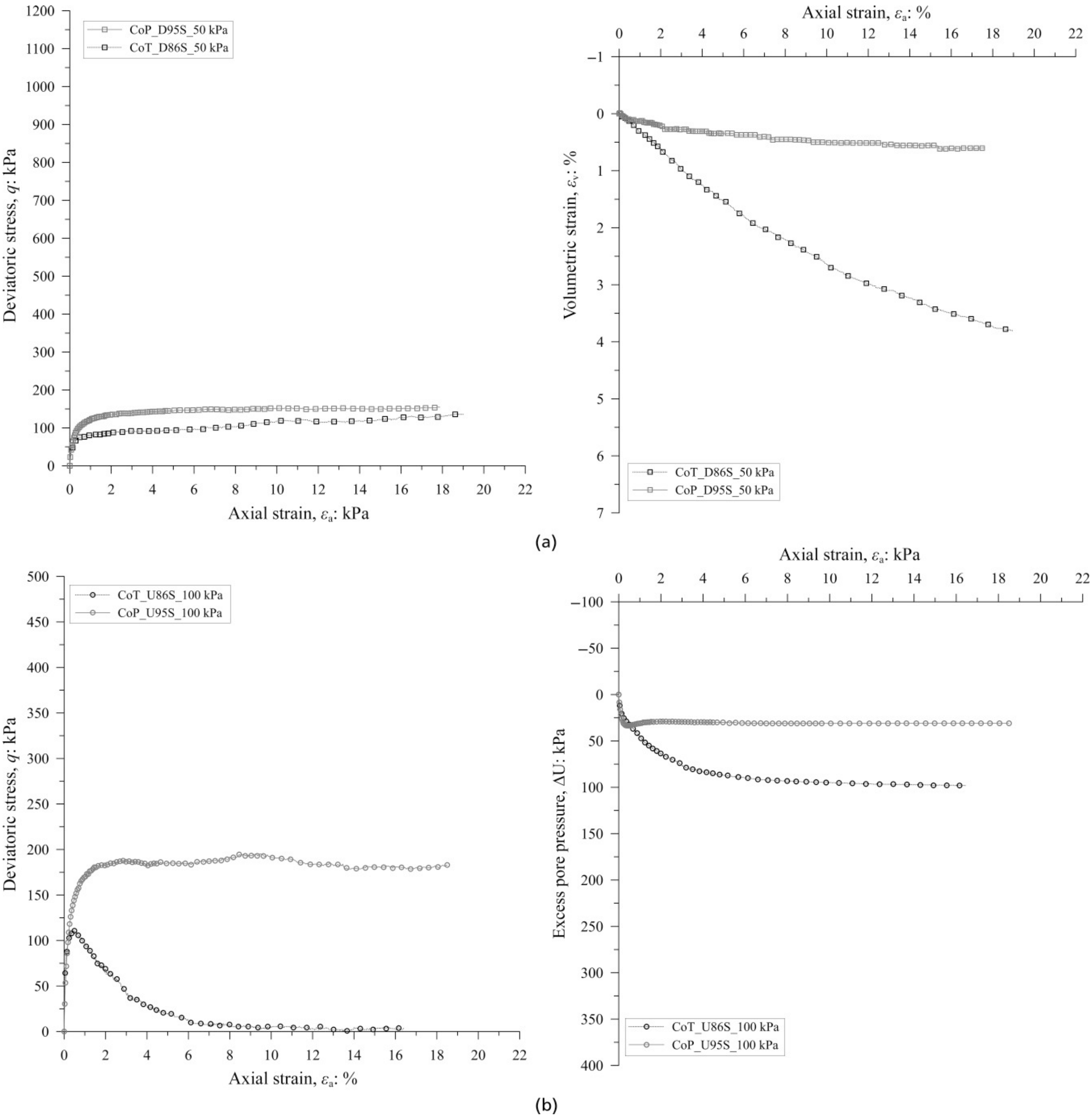

Fig. 6. Comparison of CoT and CoP tailings at a same void ratio prior to shearing under (a) drained and (b) undrained triaxial compression loading

Wagner *et al.* (2023) studied two iron ore tailings with different gradings, but similar mineralogy (both had around 75% quartz), under drained and undrained triaxial compression and extension tests, and reported non-transitional curved CSL depending on the loading type for both tailings. Although their dataset might have experienced issues with strain localisation, the possibility of achieving a unique CSL regardless of loading type is still not consensual (e.g. Riemer & Seed, 1997; Fotovvat & Sadrekarimi, 2022). Particularly for tailings, Fanni *et al.* (2024) reported a unique CSL for gold tailings tested under different loading modes with the hollow cylinder apparatus, and Becker *et al.* (2023) found a unique CSL for triaxial compression and extension. Here, CoP tailings presented loading-independent CSL, while CoT does not. These divergences in observed behaviour can be related not only to the existence of multiple CSLs but to the attainability of a unique CSL under conventional stresses and strains. It is possible that, for some strong forms of fabric, the conditions imposed in conventional tests would not be sufficient to erase the initial fabric influence. Still, the strains applied in laboratory tests tend to be much higher than those expected to occur in the field. Thus, acknowledging the unattainability of a unique CSL might provide enhanced predictions in particular cases.

Regarding the transitional response of CoT tailings, the exact cause of 'transitional' behaviour remains unknown (Coop, 2015). However, the non-transitional behaviour found for both copper tailings under simple shear conditions suggests that this stress path could lead to a higher destructuring of the fabric and, consequently, to a unique CSL. Since fabric is directly linked to the particles' shape and composition, the differences in CoT and CoP particles illustrated in Figs. 10(b) and 11(b), in conjunction with the

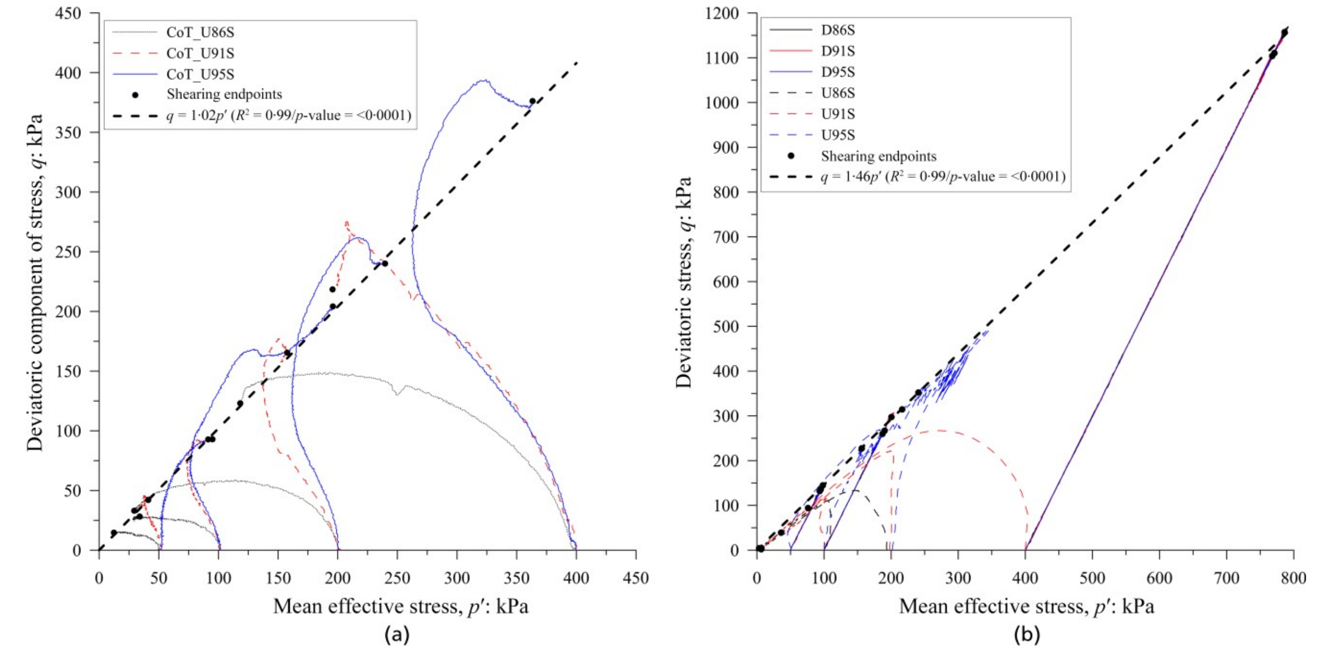

Fig. 7. Stress paths at the p'–q plane for CoT tailings: (a) simple shear tests; (b) triaxial compression tests

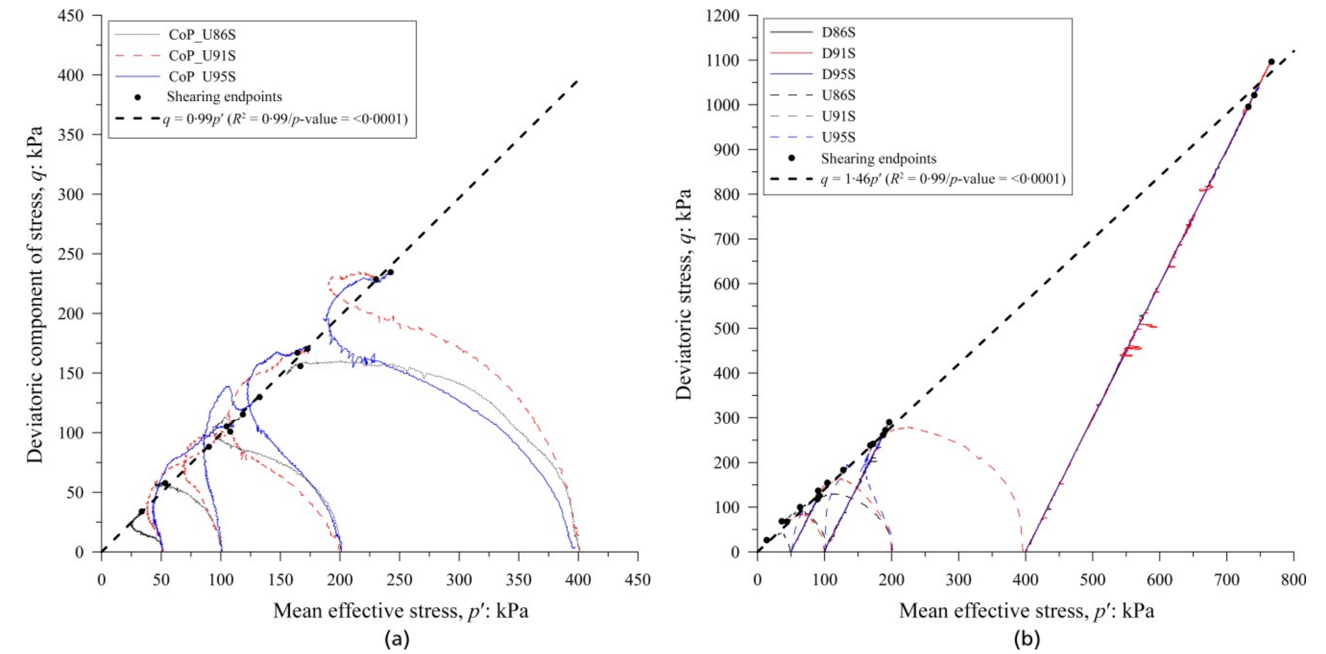

Fig. 8. Stress paths at the p'–q plane for CoP tailings: (a) simple shear tests; (b) triaxial compression tests

orientation of principal stresses in simple shear loading, might have erased the form of fabric that was originating the transitional behaviour.

Another notable difference between the investigated tailings concerns the shape of the CSL. CoT copper tailings (a quartz–feldspar dominated geomaterial) exhibited a curved CSL in the $\upsilon : log\ p'$ space for both triaxial compression and simple shear tests, whereas CoP – predominantly composed of platy minerals, such as biotite and chlorite – exhibited a loglinear CSL.

The shape of the CSL in the compression plane defines the liquefaction susceptibility of tailings. The occurrence of static liquefaction has been generally related to the curvature of the CSL (Bedin *et al.*, 2012; Carrera *et al.*, 2011; Li & Coop, 2019). Here, mineralogy has influenced the shape of the CSL despite the loading imposed or the observation of a transitional response. Although the CSL for simple shear conditions of CoT tailings was not parallel to those defined for triaxial compression, it remained curved. Conversely, the unique CSL defined for CoP tailings was loglinear for all loading types and initial densities.

Critical state lines: physical, geotechnical and mineralogical comparison between the current study and others

Figure 12 and Table 7 compare geotechnical, physical and mineralogical characteristics of the copper tailings studied herein to those of four copper tailings, two gold tailings and seven iron tailings investigated by Bedin *et al.* (2012), Li (2017), Li *et al.* (2018), Karim *et al.* (2023), Wagner *et al.* (2023), Vergaray *et al.* (2023), Consoli *et al.* (2024) and Velten *et al.* (2024). Considering only

Table 4. Calibrated parameters for the Lode-dependent strength criterion, based on Sheng *et al.* (2000) and Gajo & Muir Wood (1999)

Parameters	CoT	CoP
Dominant mineralogy	Tectosilicates (quartz and feldspar)	Phyllosilicates (biotite and chlorite)
Critical state stress ratio for triaxial compression, M_{tc}	1·46	1·40
Critical state stress ratio for simple shear, M_{ss}	1·02	0·99
M_{ss}/M_{tc}	0·70	0·71
$M(\theta)$ equation (Sheng *et al.*, 2000)	$M(\theta) = 1{\cdot}046 * \left[\frac{0{\cdot}270}{1{\cdot}135 - 0{\cdot}865 \times \sin(3\theta)}\right]^{1/4}$	$M(\theta) = 1{\cdot}40 * \left[\frac{0{\cdot}286}{1{\cdot}143 - 0{\cdot}857 \times \sin(3\theta)}\right]^{1/4}$
Predicted critical state stress ratio for triaxial extension, M_{te}	0·88	0·86
Critical state friction angle for triaxial compression, ϕ'_{tc}	36·0°	34·6°
Critical state friction angle for simple shear, ϕ'_{ss}	36·1°	34·8°

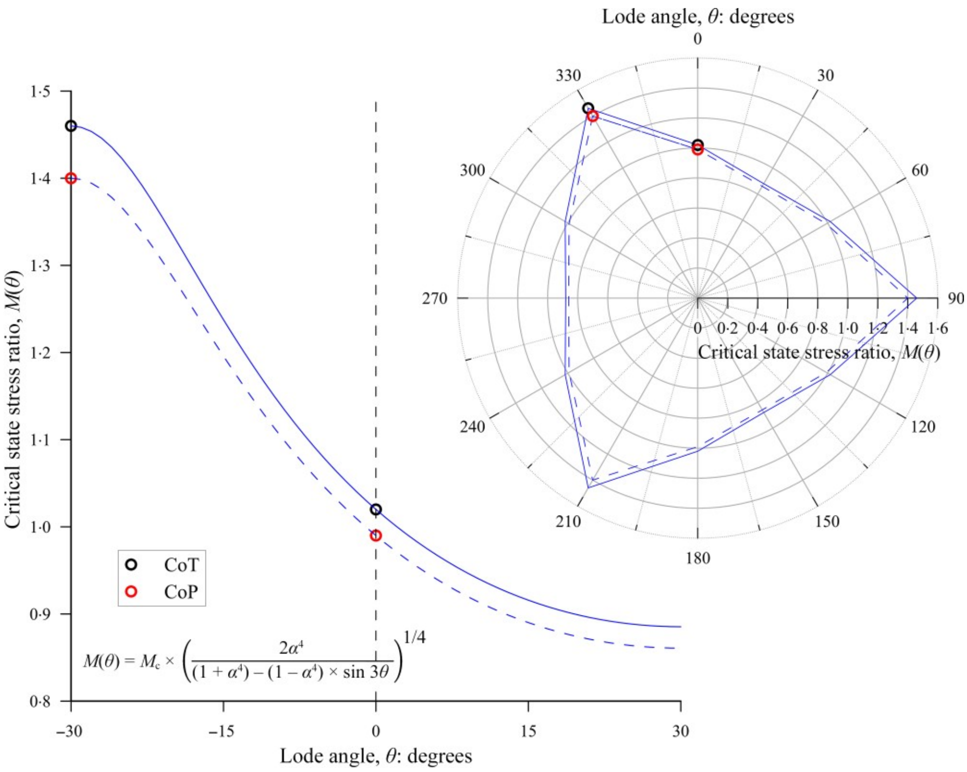

Fig. 9. Variation of the stress ratio *M* with the Lode angle *θ*. The lines represent the interpolation using the *g*(*θ*) method proposed by Sheng *et al.* (2000), calibrated with experimental data from triaxial compression (TXC) and simple shear (SS) tests

geotechnical characteristics, CoT presents gradation close to copper-lower beach from Velten *et al.* (2024), while CoP presents gradation most like gold tailings studied by Bedin *et al.* (2012), iron-flotation from Consoli *et al.* (2024) and iron-S1 from Wagner *et al.* (2023). However, under physical and mineralogical perspectives, CoT has a predominance of tectosilicate minerals (quartz and feldspar) in its internal composition, as well as most of the tailings mentioned in Fig. 12 and Table 7; however, none of them has physical and mineralogical properties comparable with CoP.

Thus, Fig. 13 and Table 8 compare the CSLs of various previously studied tailings and the copper tailings studied herein. From these results, it is observed that only CoP and iron-PO (Li, 2017) presented a linear CSL, while the others presented curved ones. Considering that, except for Deixing copper (Li, 2017), which is mainly composed of nesosilicate and considered unique in this comparison, the main minerals presented in CoP and iron-PO are phyllosilicates and inosilicates (amphibole group), respectively. So, these results confirm that mineralogy is the main reason for the CSL format, since gold tailings studied by Bedin *et al.* (2012) are coarser than gold tailings studied by Li (2017) and Li *et al.* (2018), but both presented curved CSLs and similar mineralogy.

From Fig. 13(a), it was verified that CoT presented the lower CSLs in relation to the other geomaterials, but similar curvature for the CSL obtained from triaxial compression tests. This is clearly observed from Table 8 and Fig. 13(b), which compare the CSLs obtained only for copper tailings. The location of the CSLs verified for the

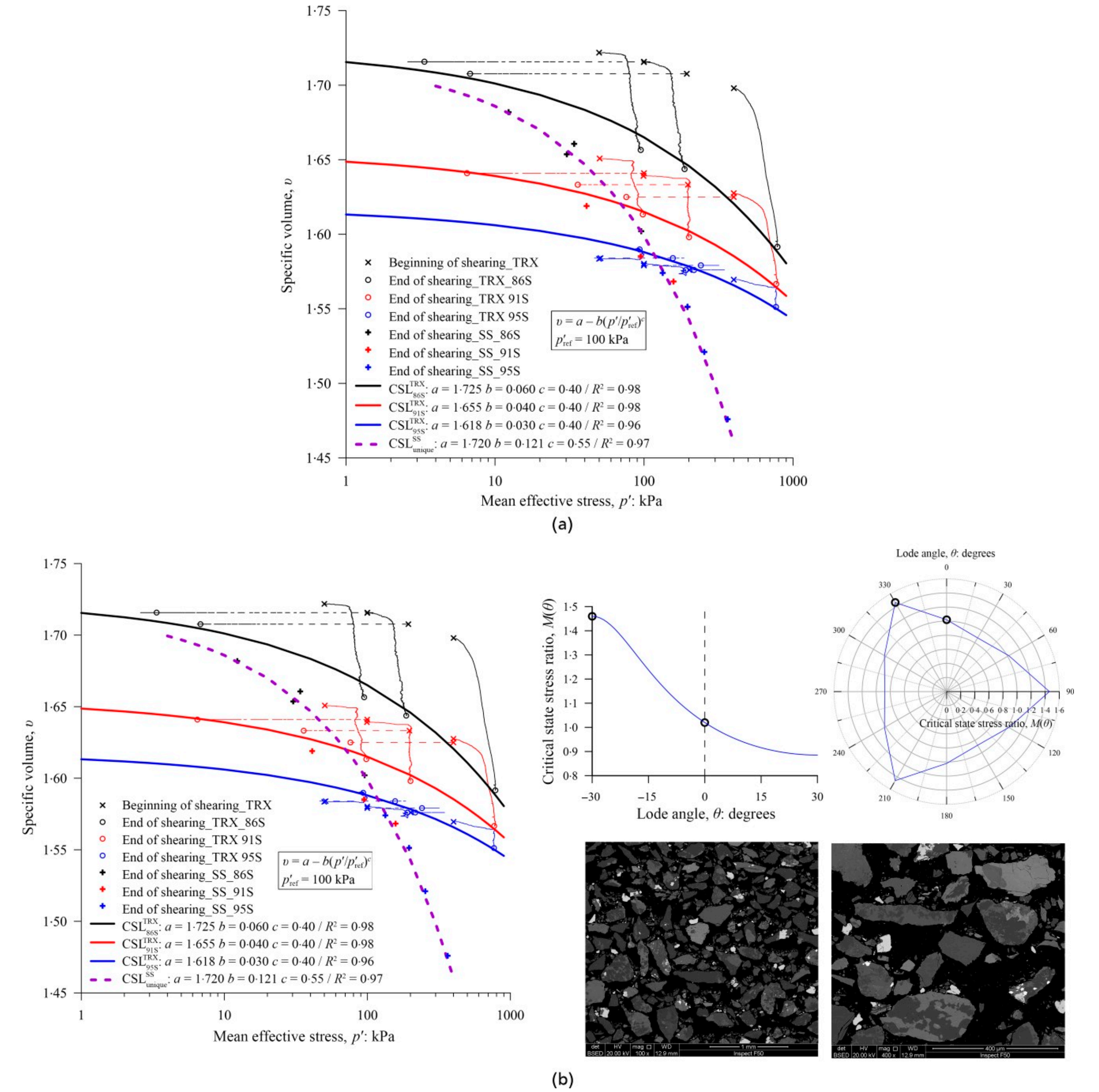

Fig. 10. (a) Critical state lines (CSLs) in the $υ$–log p' space for triaxial compression and simple shear tests – CoT. (b) CSL with SEM analysis and variation of the stress ratio M with the Lode angle θ

Table 5. Summary of CSLs obtained

Geomaterial	Dominant mineralogy	Eq. no.	Γ/λ or *a*/*b*/*c*	CSL shape	Transitional behaviour
CoT	Tectosilicates (quartz and feldspar)	(3)	Triaxial compression-86S: 1·725/0·060/0·40 Triaxial compression-91S: 1·655/0·040/0·40 Triaxial compression-95S: 1·618/0·030/0·40	Curved	Yes (TC)
			SS: 1·720/0·121/0·55	Curved	No (SS)
CoP	Phyllosilicates (biotite and chlorite)	(4)	Triaxial compression-SS: 2·053/0·074	Linear	No

Note: ‘Triaxial compression’: triaxial compression test; SS: simple shear test

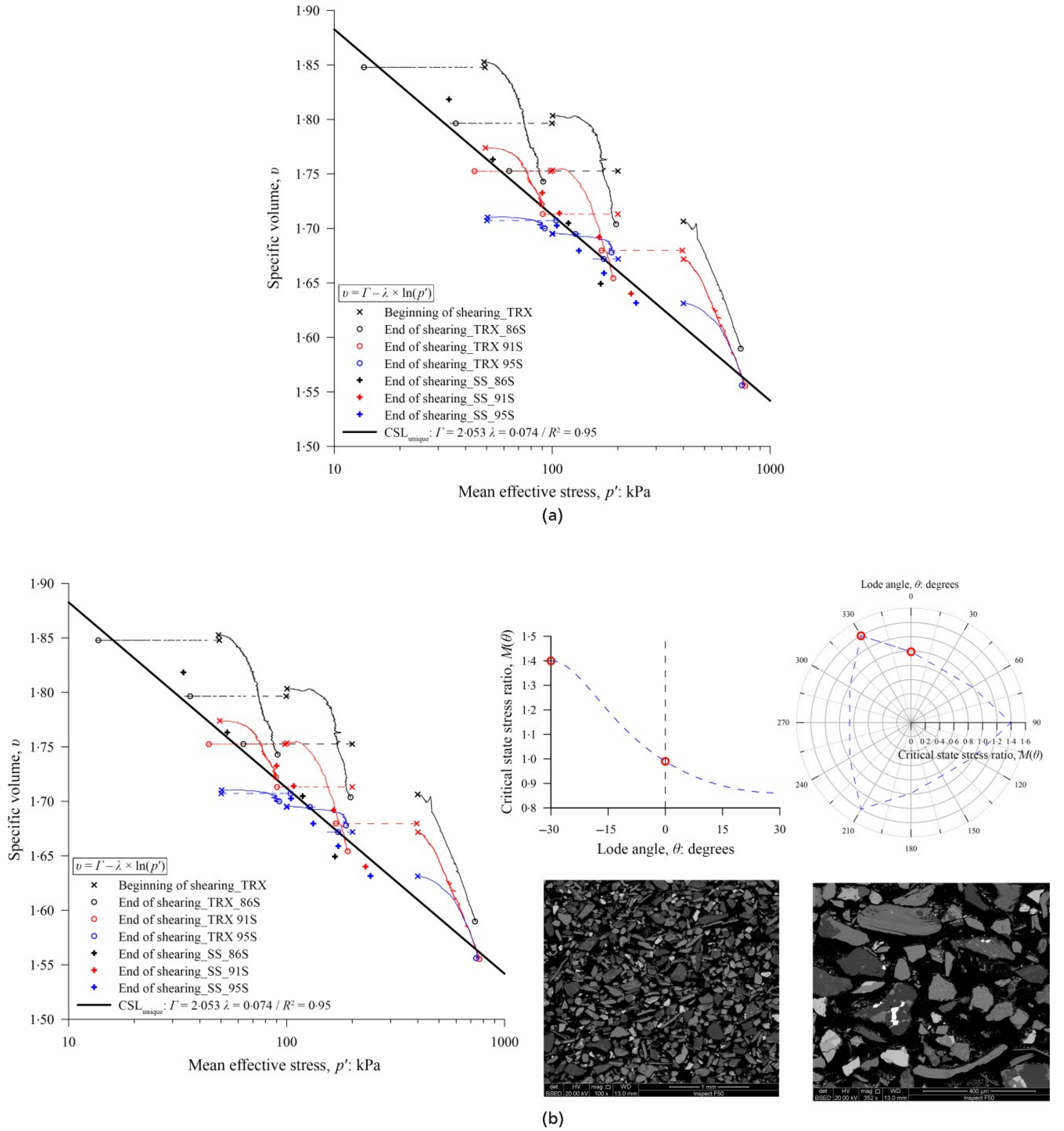

Fig. 11. (a) Critical state line (CSL) (unique) in the υ–log p' space for triaxial compression and simple shear tests – CoP. (b) CSL with SEM analysis and variation of the stress ratio M with the Lode angle θ

copper tailings studied herein, in relation to others, is wholly related to internal structure and different initial void ratios (fabric), when most researchers usually study a single initial void ratio at the loose state. Moreover, it is worth mentioning that the linear CSL of CoP crossed all the CSLs compared in Fig. 13(b), which is possibly related to its internal composition, as it is composed mainly of foliated particles (phyllosilicate minerals), which permit the rearrangement of the particles under new loading. In addition, considering that this geomaterial presented a unique CSL independently of initial void ratio and type of loading, it can be concluded that its mineralogical composition and particle packing are the main reasons for that.

When comparing the CSL obtained for copper-TSF2 (Karim *et al.*, 2023) from conventional DSS with the CSL herein obtained from SS tests (Fig. 13(c)), it was verified that the two curved CSLs are similar and they present the same curvature. Although they have gradation differences, their mineralogy is similar and mainly governed by tectosilicates (quartz and feldspar). In addition, considering that this CSL obtained from conventional DSS was calculated only using effective vertical stress, since radial stresses are not measured in this type of apparatus, they may possibly present close CSLs if they were obtained using either mean effective stress or effective vertical stress.

CONCLUDING REMARKS

The influence of mineralogy and stress path on the CSL of two copper tailings (CoT and CoP) with distinct

Table 6. Regression analysis of the CSLs

Metric	CoT				CoP
	Triaxial compression – 86S	Triaxial compression – 91S	Triaxial compression – 95S	SS	Unique
Slope (b_1)	0·9650	0·9703	0·9826	1·0357	0·9504
Intercept (b_0)	0·0585	0·0469	0·0269	−0·0548	0·0831
Standard error for slope	0·0715	0·0705	0·0904	0·0528	0·0423
Standard error for intercept	0·1189	0·1138	0·1425	0·0838	0·0719
Multiple *R*	0·9919	0·9896	0·9835	0·9873	0·9733
R^2	0·9838	0·9793	0·9672	0·9747	0·9474
Adjusted R^2	0·9784	0·9741	0·9591	0·9722	0·9455
Standard error	0·0074	0·0044	0·0027	0·0101	0·0156
Degrees of freedom – *df*	3·0000	4·0000	4·000	10·0000	28·0000
F-statistic	182·2143	189·2746	118·1156	385·0804	503·8828
p-value (*F*-test)	0·0009	0·0002	0·0004	< 0·0001	< 0·0001
Regression sums of squares	0·0096	0·0035	0·0008	0·0428	0·1164
Residual sums of square	0·0001	< 0·0001	< 0·0001	0·0011	0·0065
t-statistic (slope)	13·4987	13·7577	10·8681	19·6235	22·4473
p-value (*t*-test)	0·0009	0·0002	0·0004	< 0·0001	< 0·0001

Note: Triaxial compression: triaxial compression test; SS: simple shear test; Meaning of regression metrics: Multiple *R*: Return the correlation coefficient of the data sets; R^2 (coefficient of determination), proportion of the variance in the dependent variable explained by the model; Adjusted R^2: R^2 adjusted for the number of predictors; compensates for small sample sizes; Standard error: standard errors for *Y* estimate; *df*: degrees of freedom is the number of observations minus 2; *F*-statistic: Tests whether the regression model explains a significant amount of variance; *p*-value (*F*-test): Probability of observing the *F*-statistic if the model had no explanatory power; *t*-statistic: Tests whether an individual coefficient (e.g. slope) differs significantly from zero; and *p*-value (*t*-test): Probability of observing the *t*-statistic if the coefficient were actually zero

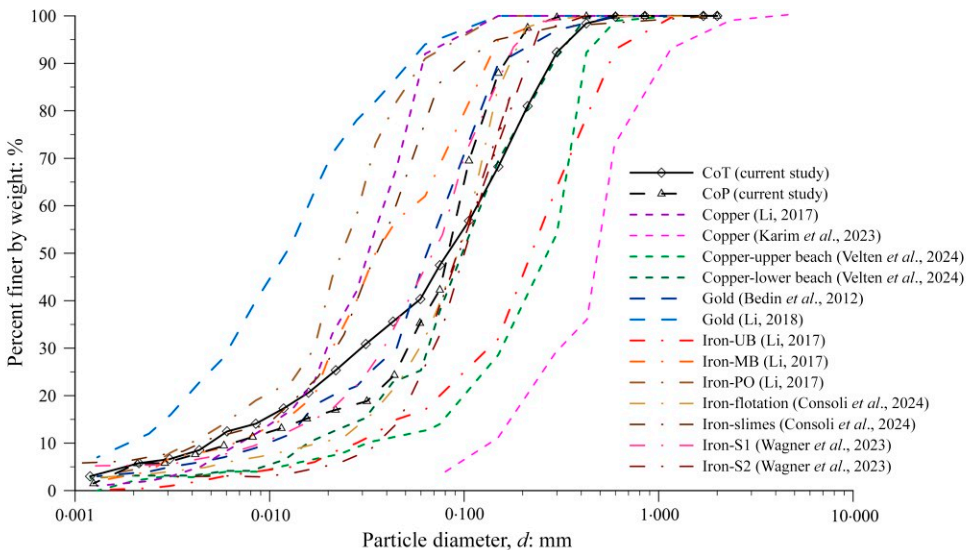

Fig. 12. Particle size distribution of various tailings samples

geological origins has been examined in this paper. Both tailings are sandy materials with similar gradings, identical D_{50} and are composed of subangular particles. However, CoT tailings are mainly composed of high-hardness minerals (quartz and feldspars), whereas CoP presents a predominance of phyllosilicate minerals, which have lower hardness. Conventional (drained and undrained) triaxial compression tests and undrained simple shear tests were compared for tailings, reflecting two different types of loading that are usually found in common TSFs. Therefore, considering the boundaries of the present research, the following conclusions can be drawn.

(*a*) CoT presented a higher critical state friction angle due to the presence of hard minerals in its constituent particles ($\phi'_{tc} = 36{\cdot}0°$ for triaxial compression and $\phi'_{ss} = 36{\cdot}1°$ for simple shear test) than CoP constituted by micaceous particles ($\phi'_{tc} = 34{\cdot}6°$ for triaxial compression and $\phi'_{ss} = 34{\cdot}8°$ for simple shear test).

(*b*) The mineralogical differences among the geomaterials studied influence their liquefaction susceptibility. For a similar void ratio, CoT tailings are more prone to liquefy and present strain-softening with positive pore pressure generation during undrained loading, while CoP tailings present a ductile and strain-hardening response, regardless of the type of loading (simple shear or triaxial compression). These differences are associated with the different CSL shapes obtained: CoT presented a curved CSL, and CoP presented a straight one.

(*c*) In triaxial compression, CoT tailings presented a 'transitional' response with multiple CSLs depending on the initial fabric, while CoP tailings do not. The transitional response was associated

Table 7. Physical, geotechnical and mineralogical characteristics of tailings – a comparison

Tailings type	FC: %	D_{50}: mm	C_u	C_{cr}	G_s	ϕ'_{cs}: deg	Main minerals	Particle shape	CSL format	Transitional behaviour
CoT –copper (current study)	47·5	0·082	26·7	1·7	2·814	36·0 (TC) / 36·1 (SS)	17·9% Qtz; 28·4% Alb; 8·3% Feld; 4·9% Bio; 10·1% Chlo; 14·2% Acti; 6·3% Mag	Massive subangular/rotund particles with some flocs around bulky particles	Curved (TC and SS)	Yes (TC) / No (SS)
CoP – copper (current study)	42·3	0·082	15·9	5·1	3·149	34·6 (TC) / 34·8 (SS)	16·4% Qtz; 4·5% Alb; 3·9% Feld; 23·6% Bio; 15·4% Chlo; 12·0% Grun; 9·1% Gar; 7·9% Mag	Subangular particles formed by stacking flocky particles (foliated particles) with some flocs bridging bulky particles	Linear (TC and SS)	No
Copper upper beach (Velten *et al*., 2024)	12·5	0·276	9·98	2·45	2·844	36·9	25·1% Qtz; 33·5% Feld; 8·4% Scp; 5·8% Amp; 5·8 Chlo; 5·3% Bio; 3·0% Mag		Curved (TC)	Yes
Copper lower beach (Velten *et al*., 2024)	25·5	0·104	8·08	2·14	2·943	35·7	25·1% Qtz; 33·5% Feld; 8·4% Scp; 5·8% Amp; 5·8 Chlo; 5·3% Bio; 3·0% Mag		Curved (TC)	Yes
Copper S1 (Vergaray *et al*., 2023)	15	0·21	4·49	—	2·70	38·0			Curved (TC)	No
Copper S2 (Vergaray *et al*., 2023)	38	0·12	11·47	—	2·60	37·8			Curved (TC)	No
Copper S3 (Vergaray *et al*., 2023)	75	0·05	13·90	—	2·75	36·6			Curved (TC)	No
Copper TSF2 (Karim *et al*., 2023)	3	0·482	3·6	1·39	2·682	28·0	32% Qtz; 30% Alb; 23% Mu3T; 12% Micr; 2% Kaol; 1% clin	Angular and rough-surfaced (coarse particles) and flocky particles (finer particles)	Curved (DSS)	No
Deixing copper (Li, 2017)	95	0·031	5·1	1·5	3·75	35·2	78% Fay; 22% Mag	Angular and subangular particles, mainly platy particles in the silt size	Curved (TC)	No
Brazilian gold (Bedin *et al*., 2012)	65	0·065	6·9	2·3	2·89–3·20	33·0	27% Qtz; 25% Alb; 35% Chlo	Bulky, angular, and subangular particles with flocs around them	Curved (TC)	No
Brazilian gold (Li *et al*., 2018)	95	0·011	7·3	1·4	2·89	34·8	27% Qtz; 25% Alb; 35% Chlo	Bulky, angular, and subangular particles with flocs around them	Curved (TC)	No
Panzhihua UB – iron (Li, 2017)	19	0·220	10·4	2·6	3·37	34·6	30% Dio; 32% Lab; 11% Hrb; 9% Chlo	Bulky, angular, and subangular particles	Curved (TC)	No
Panzhihua MB – iron (Li, 2017)	68	0·035	10·0	1·1	3·14	33·7	46% Dio; 40% Lab; 6% Hrb; 5% Chlo	Bulky, angular, and subangular particles	Curved (TC)	No
Panzhihua PO — iron (Li, 2017)	93	0·023	6·7	2·2	3·11	34·8	28% Dio; 24% Lab; 22% Hrb; 16% Chlo	Bulky, angular, and subangular particles, but flatter and more elongated	Linear (TC)	No

(continued on next page)

Table 7. Continued

Tailings type	FC: %	D_{50}: mm	C_u	C_{cr}	G_s	ϕ'_{cs}: deg	Main minerals	Particle shape	CSL format	Transitional behaviour
Iron-flotation (Consoli *et al.*, 2024)	38·6	0·094	6·5	1·87	2·83	32·2	98·3% Qtz; 1·7% Haema		Curved (TC)	No
Iron-slimes (Consoli *et al.*, 2024)	86·2	0·036	9·3	2·15	4·02	33·4	54·8% Qtz; 42·3% Haema; 2·9% Kaol		Curved (TC)	No
Iron-S1 (Wagner *et al.*, 2023)	52·2	0·068	8·8	1·80	3·05	34·6 (TC) / 35·8 (TE)	76·2% Qtz; 20·9% Ioxi	Higher quantities of bulky particles (large, subangular and subrounded shape) surrounded by flocs (collections of clay-sized particles).	Curved (TC and TE)	No
Iron-S2 (Wagner *et al.*, 2023)	33·3	0·100	3·2	0·90	2·97	33·4 (TC) / 34·8 (TE)	78·4% Qtz; 17·2% Ioxi	Higher quantities of bulky particles (large, subangular and subrounded shape)	Curved (TC and TE)	No

Note: FC, fine content; D_{50}, mean particle size; C_u, uniformity coefficient; C_{cr}, coefficient of curvature; G_s, specific gravity; ϕ'_{cs}, critical state friction angle; TC, triaxial compression; DSS, direct simple shear; SS, simple shear; Minerals: Qtz, quartz (tectosilicate); Feld, feldspar (tectosilicate); Alb, albite (feldspar group – tectosilicate); Lab, Labradorite (feldspar group – tectosilicate); Micr. microcline (feldspar group – tectosilicate); Scp, scapolite (tectosilicate); Mu3T, muscovite-3T (mica group – phyllosilicate); Chl, chlorite (chlorite group – phyllosilicate); Clin, clinochlore (chlorite group – phyllosilicate); Bio, biotite (mica group – phyllosilicate); Kaol, kaolinite (clay group – phyllosilicate); Acti, actinolite (amphibole group – inosilicate double chain); Grun, grunerite (amphibole group – inosilicate double chain); Amp, amphibole (inosilicate double chain); Hrb, hornblende (amphibole group – inosilicate double chain); Dio, diopside (pyroxene group – inosilicate single chain); Gar, garnet (nesosilicate); Fay, fayalite (olivine group – nesosilicate); Mag, magnetite (iron oxide); Haem, haematite (iron oxide); Ioxi, iron oxide; Cal, calcite (calcium carbonate); Dol, dolomite (calcium–magnesium carbonate)

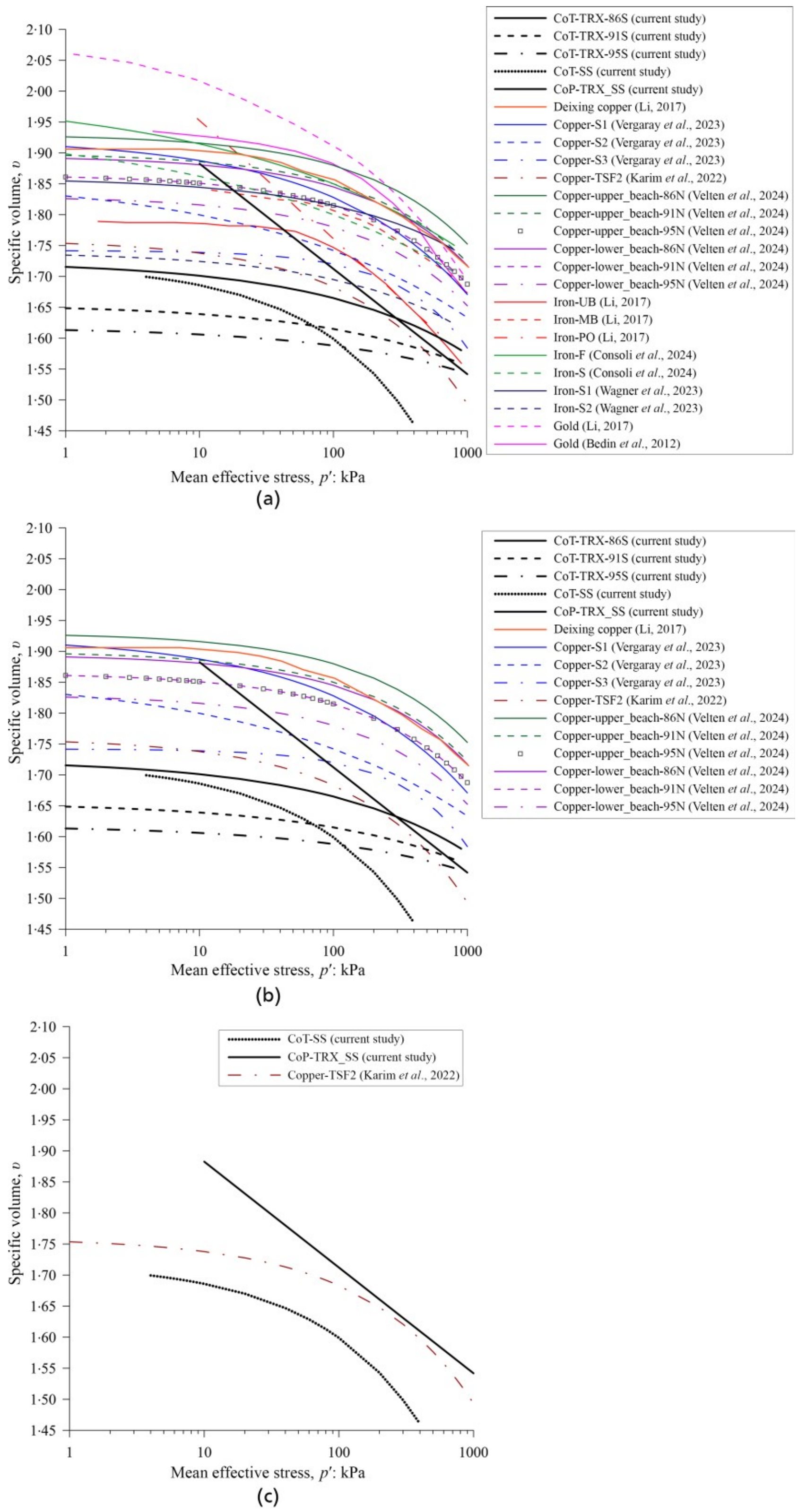

Fig. 13. Critical state line (CSL) of various tailings samples for comparison: (a) all tailings samples; (b) only copper tailings; and (c) only CSLs obtained from SS or DSS tests

with strong forms of fabric that could not be completely erased under conventional triaxial conditions. Although the exact element of fabric causing transitionality could not be identified, mineralogy exerted an influence on this response since both tailings presented similar gradings and were tested under the same conditions.

(*d*) Comparison of triaxial compression with published simple shear results on the same tailings indicates distinct responses for CoT and CoP. While CoT presented a stress path-dependent CSL, CoP presented a unique CSL regardless of the loading path. The mechanism underlying this difference can be the same as that for transitionality. Regardless of whether a unique

Table 8. Critical state lines (CSLs) properties of tailings geomaterials

Tailings type	FC: %	Γ / ℓ	*a*/*b*/*c*	G_s	M	Main minerals	Transitional behaviour
CoT – copper (current study)	47·5		86S: 1·725/0·060/0·40 91S: 1·655/0·040/0·40 95S: 1·618/0·030/0·40 1·720/0·121/0·55	2·814	1·46 (TC) 1·02 (SS)	17·9% Qtz; 28·4% Alb; 8·3% Feld; 4·9% Bio; 10·1% Chlo; 14·2% Acti; 6·3% Mag	Yes (TC)/No (SS)
CoP – copper (current study)	42·3	2·053/0·074		3·149	1·40 (TC)/0·99 (SS)	16·4% Qtz; 4·5% Alb; 3·9% Feld; 23·6% Bio; 15·4% Chlo; 12·0% Grun; 9·1% Gar; 7·9% Mag	No
Copper upper beach (Velten *et al.*, 2024)	12·5		86 N: 1·93/0·05/0·55 91 N: 1·90/0·05/0·55 95 N: 1·865/0·05/0·55	2·844	1·50 (TC)	25·1% Qtz; 33·5% Feld; 8·4% Scp; 5·8% Amp; 5·8 Chlo; 5·3% Bio; 3·0% Mag	Yes
Copper lower beach (Velten *et al.*, 2024)	25·5		86 N: 1·895/0·05/0·55 91 N: 1·865/0·05/0·55 95 N: 1·830/0·05/0·55	2·943	1·40 (TC)	25·1% Qtz; 33·5% Feld; 8·4% Scp; 5·8% Amp; 5·8 Chlo; 5·3% Bio; 3·0% Mag	Yes
Copper S1 (Vergaray *et al.*, 2023)	15	2·013/0·045	1·924/0·096/0·421	2·70	1·55 (TC)		No
Copper S2 (Vergaray *et al.*, 2023)	38	1·876/0·033	1·865/0·123/0·275	2·60	1·54 (TC)		No
Copper S3 (Vergaray *et al.*, 2023)	75	1·860/0·033	1·742/0·022/0·856	2·75	1·49 (TC)		No
Copper TSF2 (Karim *et al.*, 2023)	3	—	1·76/0·0769/0·54	2·682	$(\tau/\sigma'_N)_{CS}$ = 0·53 (DSS)	32% Qtz; 30% Alb; 23% Mu3T; 12% Micr; 2% Kaol; 1% clin	No
Deixing copper (Li, 2017)	95	1·84 (Γ_{100})/0·126	1·92/0·070/0·42	3·75	1·43 (TC)	78% Fay; 22% Mag	No
Brazilian gold (Bedin *et al.*, 2012)	65	1·89 (Γ_{100})/0·206	1·955/0·070/0·65	2·89–3·20	1·33 (TC)	27% Qtz; 25% Alb; 35% Chlo	No
Brazilian gold (Li *et al.*, 2018)	95	1·89 (Γ_{100})/0·176	2·150/0·25/0·25	2·89	1·41 (TC)	27% Qtz; 25% Alb; 35% Chlo	No
Panzhihua UB – iron (Li, 2017)	19	1·79 (Γ_{100})/0·252	1·795/0·090/0·39	3·37	1·41 (TC)	30% Dio; 32% Lab; 11% Hrb; 9% Chlo	No
Panzhihua MB – iron (Li, 2017)	68	1·81 (Γ_{100})/0·152	1·875/0·080/0·39	3·14	1·36 (TC)	46% Dio; 40% Lab; 6% Hrb; 5% Chlo	No
Panzhihua PO — iron (Li, 2017)	93	1·76 (Γ_{100})/0·185		3·11	1·40 (TC)	28% Dio; 24% Lab; 22% Hrb; 16% Chlo	No
Iron-flotation (Consoli *et al.*, 2024)	38·6		2·00/0·15/0·245	2·83	1·30 (TC)	98·3% Qtz; 1·7% Haema	No
Iron-slimes (Consoli *et al.*, 2024)	86·2		1·95/0·15/0·232	4·02	1·35 (TC)	54·8% Qtz; 42·3% Haema; 2·9% Kaol	No
Iron-S1 (Wagner *et al.*, 2023)	52·2		1·86/0·045/0·46	3·05	1·40 (TC)/0·98 (TE)	76·2% Qtz; 20·9% Ioxi	No
Iron-S2 (Wagner *et al.*, 2023)	33·3		1·74/0·045/0·46	2·97	1·35 (TC)/0·96 (TE)	78·4% Qtz; 17·2% Ioxi	No

Note: FC, fine content; Γ_{100}, intercept of CSL at p'= 100 kPa; Γ, intercept of linear CSL at p'= 1·0 kPa; ℓ, slope of linear CSL; *a*, intercept of curved CSL at p' = 1·0 kPa; *b*, slope of curved CSL; *c*, exponent of curved CSL; G_s, specific gravity; ϕ'_{cs}, critical state friction angle; TC, triaxial compression; DSS, direct simple shear; SS, simple shear; Minerals: Qtz, quartz (tectosilicate); Feld, feldspar (tectosilicate); Alb, albite (feldspar group – tectosilicate); Lab, Labradorite (feldspar group – tectosilicate); Micr., microcline (feldspar group – tectosilicate); Scp, scapolite (tectosilicate); Mu3T, muscovite-3T (mica group – phyllosilicate); Chl, chlorite (chlorite group – phyllosilicate); Clin, clinochlore (chlorite group – phyllosilicate); Bio, biotite (mica group – phyllosilicate); Kaol, kaolinite (clay group – phyllosilicate); Acti, actinolite (amphibole group – inosilicate double chain); Grun, grunerite (amphibole group – inosilicate double chain); Amp, amphibole (inosilicate double chain); Hrb, hornblende (amphibole group – inosilicate double chain); Dio, diopside (pyroxene group – inosilicate single chain); Gar, garnet (nesosilicate); Fay, fayalite (Olivine group – nesosilicate); Mag, magnetite (iron oxide); Haem, haematite (iron oxide); Ioxi, Iron oxide; Cal, calcite (calcium carbonate); Dol, dolomite (calcium–magnesium carbonate)

CSL exists, strong forms of fabric might prevent its attainability under conventional stresses and strains. In this sense, the simple shear loading appears to be more effective in destructuration. This effect can also be observed in transitionality. Despite presenting a transitional response in triaxial compression, CoT presented a density-independent CSL under simple shear loading.

The present findings demonstrate the importance of investigating how mineralogy influences the fabric dependence of tailings under different stress paths, providing new insights into the cause of transitional behaviour. In this way, more research is required using other types of loading, for example, hollow cylinder tests with various stress paths, since TSFs can be submitted to all types of stress paths during their life cycle. Besides, a pivotal aspect of future research will be to increase the level of stress applied, since some TSFs and other earthworks can often be submitted to stresses higher than 1000 kPa.

DECLARATIONS

CONFLICT OF INTEREST

The authors declare that they have no known competing financial interests or personal relationships that could have appeared to influence the work reported in this paper.

DATA AVAILABILITY

Some or all the data, models, or codes used in this research can be made available by the corresponding author upon reasonable request.

ACKNOWLEDGEMENTS

The authors wish to thank MCT-CNPq (Editais INCT-REAGEO, Universal & Produtividade em Pesquisa), Vale S. A. (Laboratório de Mineralogia, Centro de Desenvolvimento Mineral) and Vale Base Metals S.A. (VALE BMSA) for supporting the research group. This study was financed by the Coordenação de Aperfeiçoamento de Pessoal de Nível Superior – Brasil (CAPES) – PROEX and Finance Code 001. The authors wish to thank Dr Hugo Carlos Scheuermann Filho, from Universidade Federal do Rio Grande do Sul (UFRGS), for his valuable contributions to this paper.

NOTATION

- a the intercept at 1 kPa of a curved critical state line (CSL) (in the υ−ln p' space)
- b the gradient of a curved CSL (in the υ−ln p' space)
- c the adjustment exponent of a curved CSL (in the υ−ln p' space)
- e void ratio
- G_s specific gravity
- M critical state stress ratio (in the p'–q space)
- M_{ss} critical state stress ratio (in the p'–q space) for simple shear tests
- M_{tc} critical state stress ratio (in the p'–q space) for triaxial compression tests
- p' mean effective stress
- p'_0 initial mean effective stress (just before shearing)
- q deviatoric stress – triaxial test ($\sigma_1 - \sigma_3$)
- q_{ss} deviatoric component of stress – simple shear test $\left(q_{ss} = \frac{1}{\sqrt{2}} \times \sqrt{(\sigma'_1 - \sigma'_2)^2 + (\sigma'_1 - \sigma'_3)^2 + (\sigma'_2 - \sigma'_3)^2}\right)$
- u pore water pressure
- w water content
- Γ the intercept at 1 kPa of a straight CSL (in the υ−ln p' space)
- ε_s shear strain
- η stress ratio = q/p'
- θ Lode's angle
- λ gradient of a linear CSL (in the υ−ln p' space)
- σ'_h effective horizontal stress
- σ'_v effective vertical stress
- σ_1, σ_3 principal stresses
- τ shear stress
- υ specific volume = 1 + e
- ϕ' effective stress friction angle
- ϕ'_{cs} critical state friction angle
- ϕ'_{peak} peak friction angle
- ψ state parameter

REFERENCES

ASTM (2014). ASTM D854: Test methods for specific gravity of soil solids by water pycnometer. ASTM International, West Conshohocken, PA, USA.

ASTM (2017a). ASTM D6913: Test methods for particle-size distribution (gradation) of soils using sieve analysis. ASTM International, West Conshohocken, PA, USA.

ASTM (2017b). ASTM D4318: Standard test methods for liquid limit, plastic limit, and plasticity index of soils. ASTM International, West Conshohocken, PA, USA.

ASTM (2017c). ASTM D2487: Practice for classification of soils for engineering purposes (Unified Soil Classification System). ASTM International, West Conshohocken, PA, USA.

ASTM (2020a). ASTM D7181: Standard test method for consolidated drained triaxial compression test for soils. ASTM International, West Conshohocken, PA, USA.

ASTM (2020b). ASTM D4767: Standard test method for consolidated undrained triaxial compression test for cohesive soils. ASTM International, West Conshohocken, PA, USA.

ASTM (2021a). ASTM D7928: Standard test method for particle-size distribution (gradation) of fine-grained soils using the sedimentation (hydrometer) analysis. ASTM International, West Conshohocken, PA, USA.

ASTM (2021b). ASTM D698: Standard test method for laboratory compaction characteristics of soil using standard effort (12,400 ft-lbf/ft3 (600 kN-m/m3)). ASTM International, West Conshohocken, PA, USA.

ASTM (2021c). ASTM D1557: Standard test method for laboratory compaction characteristics of soil using modified effort (56,000 ft-lbf/ft3 (2700 kN-m/m3)). ASTM International, West Conshohocken, PA, USA.

Becker, L. D. B., Fabre, J. S. & Barbosa, M. C. (2023). Determination of the critical state of a silty sand iron tailings in triaxial extension tests using photographic correction. *Can. Geotech. J.* **60**, No. 4, 504–520, 10.1139/cgj-2021-0637.

Bedin, J., Schnaid, F., DA Fonseca, A. V. & Costa Filho, L. M. (2012). Gold tailings liquefaction under critical state soil mechanics. *Géotechnique* **62**, No. 3, 263–267, 10.1680/geot.10.P.037.

Bolton, M. D. (1986). The strength and dilatancy of sands. *Géotechnique* **36**, No. 1, 65–78, 10.1680/geot.1986.36.1.65.

Bowker, L. & Chambers, D. (2017). In the dark shadow of the supercycle tailings failure risk & public liability reach all-time highs. *Environments* **4**, No. 4, 75, 10.3390/environments4040075.

Byrne, P., Hudson-Edwards, K. A., Bird, G., Macklin, M. G., Brewer, P. A., Williams, R. D. & Jamieson, H. E. (2018). Water quality impacts and river system recovery following the 2014 Mount Polley mine tailings dam spill, British Columbia, Canada. *Appl. Geochem.* **91**, 64–74, 10.1016/j.apgeochem.2018.01.012.

Carrera, A., Coop, M. & Lancellotta, R. (2011). Influence of grading on the mechanical behaviour of Stava tailings. *Géotechnique* **61**, No. 11, 935–946, 10.1680/geot.9.P.009.

Chang, N., Heymann, G. & Clayton, C. (2011). The effect of fabric on the behaviour of gold tailings. *Géotechnique* **61**, No. 3, 187–197, 10.1680/geot.9.P.066.

Clayton, C. R. I. & Khatrush, S. A. (1986). A new device for measuring local axial strains on triaxial specimens. *Géotechnique* **36**, No. 4, 593–597, 10.1680/geot.1986.36.4.593.

Consoli, N. C., Silva, J. P. S., Wagner, A. C., Carvalho, J. V. A., Baudet, B. A., Coop, M. R., Scheuermann Filho, H. C., Carvalho, I., Marçal de Sousa, G. & Cacciari, P. P. (2024). Critical state analysis of two compacted filtered iron ore tailings with different gradings and mineralogy at different stages of treatment. *Acta Geotech.* **19**, No. 2, 881–898, 10.1007/s11440-023-01963-9.

Coop, M. R. (2015). Limitations of a critical state framework applied to the behaviour of natural and 'transitional' soils. *Proceedings of the 6th international symposium on deformation characteristics of geomaterials*, Buenos Aires, Argentina.

Corrêa, M. M. & Oliveira Filho, W. L. (2019). Impact of methods used to reconstitute tailings specimens on the liquefaction potential assessment of tailings dams. *REM, Int. Engng J.* **72**, No. 3, 507–513, 10.1590/0370-44672018720164.

Doherty, J. & Fahey, M. (2011). Three-dimensional finite element analysis of the direct simple shear test. *Comput. Geotech.* **38**, No. 7, 917–924, 10.1016/j.compgeo.2011.05.005.

Fanni, R., Reid, D. & Fourie, A. B. (2024). Effect of principal stress direction on the instability of sand under the constant shear drained stress path. *Géotechnique* **74**, No. 9, 875–891, 10.1680/jgeot.22.00062.

Fotovvat, A. R. & Sadrekarimi, A. (2022). Instability of a gold mine tailings subjected to different stress paths. *J. Geotech. Geoenviron. Engng* **148**, No. 5, 04022020, 10.1061/(ASCE)GT.1943-5606.0002780.

Frost, J. & Park, J. Y. (2003). A critical assessment of the moist tamping technique. *Geotech. Test. J.* **26**, No. 1, 57–70, 10.1520/gtj11108j.

Gajo, A. & Muir Wood, D. (1999). Severn–Trent sand: a kinematic-hardening constitutive model: the q–p' formulation. *Géotechnique* **49**, No. 5, 595–614, 10.1680/geot.1999.49.5.595.

Islam, K. & Murakami, S. (2021). Global-scale impact analysis of mine tailings dam failures: 1915–2020. *Glob. Environ. Change* **70**, 102361, 10.1016/j.gloenvcha.2021.102361.

Karim, M. E., Rahman, M. M., Karim, M. R., Fourie, A. B. & Reid, D. (2023). Characteristics of copper tailings in direct simple shearing: a critical state approach. *J. Geotech. Geoenviron. Engng* **149**, No. 5, 04023018, 10.1061/JGGEFK.GTENG-11031.

Ladd, R. S. (1978). Preparing tests specimens using undercompaction. *Geotech. Test. J.* **1**, No. 1, 16–23, 10.1520/GTJ10364J.

Li, W. (2017). *The mechanical behaviour of tailings*. PhD thesis, City University of Hong Kong.

Li, W. & Coop, M. R. (2019). Mechanical behaviour of Panzhihua iron tailings. *Can. Geotech. J.* **56**, No. 3, 420–435, 10.1139/cgj-2018-0032.

Li, W., Coop, M. R., Senetakis, K. & Schnaid, F. (2018). The mechanics of a silt-sized gold tailing. *Engng Geol.* **241**, 97–108, 10.1016/j.enggeo.2018.05.014.

Matsuoka, H. & Nakai, T. (1974). Stress-deformation and strength characteristics of soil under three different principal stresses. *Proc. Japan. Soc. Civ. Engrs*, No. 232, 59–70, 10.2208/jscej1969.1974.232_59.

Murthy, T. G., Loukidis, D., Carraro, J. A. H., Prezzi, M. & Salgado, R. (2007). Undrained monotonic response of clean and silty sands. *Géotechnique* **57**, No. 3, 273–288, 10.1680/geot.2007.57.3.273.

Nakata, Y., Kato, Y., Hyodo, M., Hyde, A. F. L. & Murata, H. (2001). One-dimensional compression behaviour of uniformly graded sand related to single particle crushing strength. *Soils Found.* **41**, No. 2, 39–51, 10.3208/sandf.41.2_39.

Nocilla, A., Coop, M. R. & Colleselli, F. (2006). The mechanics of an Italian silt: an example of 'transitional' behaviour. *Géotechnique* **56**, No. 4, 261–271, 10.1680/geot.2006.56.4.261.

Nocilla, A., Ponzoni, E., Zimbardo, M. & Coop, M. R. (2019). The role of particle mineralogy in mixtures of sands. *Proceedings of the XVII ECSMGE-2019: Geotechnical engineering, foundation of the future*. 10.32075/17ECSMGE-2019-0824.

Reid, D., Fourie, A., Ayala, J. L., Dickinson, S., Ochoa-Cornejo, F., Fanni, R., Garfias, J., Viana da Fonseca, A., Ghafghazi, M., Ovalle, C., Riemer, M., Rismanchian, A., Olivera, R. & Suazo, G. (2021). Results of a critical state line testing round robin programme. *Géotechnique* **71**, No. 7, 616–630, 10.1680/jgeot.19.P.373.

Riemer, M. F. & Seed, R. B. (1997). Factors affecting apparent position of steady-state line. *J. Geotech. Geoenviron. Engng 123* **123**, No. 3, 281–288, 10.1061/(ASCE)1090-0241(1997)123:3(281).

Riveros, G. A. & Sadrekarimi, A. (2021). Static liquefaction behaviour of gold mine tailings. *Can. Geotech. J.* **58**, No. 6, 889–901, 10.1007/s10706-016-0033-7.

Sadrekarimi, A. (2016). Static liquefaction analysis considering principal stress directions and anisotropy. *Geotech. Geol. Engng* **34**, No. 4, 1135–1154, 10.1007/s10706-016-0033-7.

Secco, M. P., Carvalho, J. V. A., Wagner, A. C., Guedes, J. P. C., Silva, J. P. S. & Consoli, N. C. (2026). How particle breakage affects the critical state line of silty-sand iron tailings. *Acta Geotech.* **21**, No. 4, 2009–2022, 10.1007/s11440-025-02901-7.

Seethalakshmi, P. & Sachan, A. (2020). A comparative study on shear behavior of pure sand and micaceous sand under undrained monotonic and dynamic loading conditions. In *Advances in computer methods and geomechanics* (eds A. Prashant, A. Sachan and C. S. Desai), pp. 49–66. Singapore: Springer Singapore.

Sheng, D., Sloan, S. W. & Yu, H. S. (2000). Aspects of finite element implementation of critical state models. *Comput. Mech.* **26**, No. 2, 185–196, 10.1007/s004660000166.

Shipton, B. & Coop, M. R. (2015). Transitional behaviour in sands with plastic and non-plastic fines. *Soils Found.* **55**, No. 1, 1–16, 10.1016/j.sandf.2014.12.001.

Sladen, J. A. & Handford, G. (1987). A potential systematic error in laboratory testing of very loose sands. *Can. Geotech. J.* **24**, No. 3, 462–466, 10.1139/t87-058.

Teixeira, J. B. & Lindenmayer, Z. G. (2012). Serra dos Carajás. In *Geologia do Brasil* (eds Y. Hasui, C. D. R. Carneiro, F. D. M. Almeida and A. Bartorelli). São Paulo, Brazil: Editora Beca.

Velten, R. Z., Consoli, N. C., Scheuermann Filho, H. C., Wagner, A. C., Schnaid, F. & Da Costa, J. P. R. (2024). Influence of grading and fabric arising from the initial compaction on the geomechanical characterisation of compacted copper tailings. *Géotechnique* **74**, No. 5, 461–472, 10.1680/jgeot.22.00087.

Velten, R. Z., Ulsen, C., Da Costa, J. P. R., Lima, C. A. A., Mafessoli, M., Carvalho, J. V. A. & Consoli, N. C. (2025). Role of mineralogy on the undrained monotonic simple shear response of compacted filtered copper tailings. *Soils Found.* **65**, No. 4, 101636, 10.1016/j.sandf.2025.101636.

Vergaray, L., Macedo, J. & Arnold, C. (2023). Static and cyclic liquefaction of copper mine tailings. *J. Geotech. Geoenviron. Engng* **149**, No. 5, 10.1061/jggefk.gteng-10661.

Wagner, A. C., Silva, J. P. S., Carvalho, J. V. A., Rissoli, A. L. C., Cacciari, P. P., Chaves, H. M., Scheuermann Filho, H. C. & Consoli, N. C. (2023). Mechanical behavior of iron ore tailings under standard compression and extension triaxial stress paths. *J. Rock Mech. Geotech. Engng* **15**, No. 7, 1883–1894, 10.1016/j.jrmge.2022.11.013.

Wagner, A. C., Carvalho, J. V. A., Silva, J. P. S., Scheuermann Filho, H. C. & Consoli, N. C. (2024). Dry stacking of iron ore tailings: Possible particle breakage during compaction. *Proc. Instn Civ. Engrs — Geotech. Engng* **177**, No. 6, 779–787, 10.1680/jgeen.22.00216.

Wagner, A. C., Carvalho, J. V. A., Scheuermann Filho, H. C. & Consoli, N. C. (2025). Influence of grading in compacted tailings behaviour: towards resilient design. *Géotechnique* **75**, No. 13, 150–163, 10.1680/jgeot.23.00475.

Wroth, C. P. (1984). The interpretation of in situ soil tests. *Géotechnique* **34**, No. 4, 449–489, 10.1680/geot.1984.34.4.449.

Zhang, J., Liu, X., Gao, H., Wang, G., An, R. & Liang, Z. (2024). Impact of mica on geotechnical behavior of weathered granitic soil using macro and micro investigations. *J. Rock Mech. Geotech. Engng* **16**, No. 6, 2250–2266, 10.1016/j.jrmge.2023.03.011.

Zhang, X., Baudet, B. A. & Yao, T. (2020). The influence of particle shape and mineralogy on the particle strength, breakage and compressibility. *Geo-Engineering* **11**, No. 1, 10.1186/s40703-020-0108-4.